DISG: Driving-Integrated Spherical Gear Enables Singularity-Free Full-Range Joint Motion

Guanqi Liang, *Student Member, IEEE,* Lijun Zong, *Member, IEEE,* and Tin Lun Lam, *Senior Member, IEEE*

***Abstract*—Dexterous joints have attracted interest in the field of robotics. This paper presents a driving-integrated spherical gear (DISG) that enables entire spherical meshing and active driving between two spherical gears, forming a dexterous multi-DoF rolling contact joint. The driving-integrated spherical gear consists of a pair of spherical gears and an omnidirectional internal driver. The spherical gear shape is a combined projection of the conventional planar gear profile in the longitudinal and latitudinal directions, which can mesh and be driven over the entire sphere. An actively driving magnet and a passively following magnet are magnetically connected across the spherical gear and together form the internal driver, enabling arbitrary connection points throughout the sphere. In all configurations, one spherical gear can roll in all directions on the surface of the other. Furthermore, we analyze the kinematics of DISG and prove that the DISG-based dexterous joint has good kinematic characteristics, such as singularity-free and full-range workspace. We verify the theoretical and physical characteristics of DISG in a series of experiments on the prototype. As an extension, we implement a 3-DoF independent robotic wrist by tandemly connecting a revolute joint. We also compare DISG-based joints to other joint actuators and show that DISG-based joints have advantages in dexterity, motion range, compactness, and lightweight.**

***Index Terms*—Spherical Gear, Dexterous Joint, Kinematics Analysis, Actuator**

I. Introduction

THE spatial orientation of an end-effector is closely linked to its ability to perform the desired task, while robotic joints provide rotational degrees of freedom (DoF) for changing spatial orientation [1, 2]. Prosthetic studies suggest that increased joint dexterity can contribute more to manipulation capacity than a highly dexterous end-effector with limited joint capability [3]. Motivated by societal expectations, research on multi-DoF mechanisms, actuators, and integrated robotic joints has been ongoing [4–6]. Compared to conventional series/parallel multi-DoF mechanisms, single joints with multi-DoF offer greater dexterity, compactness, and functionality,

This work was supported in part by the National Natural Science Foundation of China under Grant 62073274; in part by the Guangdong Basic and Applied Basic Research Foundation under Grant 2023B1515020089; and in part by the Shenzhen Institute of Artificial Intelligence and Robotics for Society under Grant AC01202101103. (*Corresponding author: Tin Lun Lam.*)

Guanqi Liang and Tin Lun Lam are with the School of Science and Engineering, The Chinese University of Hong Kong, Shenzhen, Guangdong, 518172; Shenzhen Institute of Artificial Intelligence and Robotics for Society (AIRS), Shenzhen, Guangdong, 518172, P.R. China (email:guanqiliang@link.cuhk.edu.cn; tllam@cuhk.edu.cn).

Lijun Zong is with the School of Mechanical Engineering, Northwestern Polytechnical University, Xi'an, Shaanxi, 710072; The Key Laboratory of Aircraft High Performance Assembly, Ministry of Industry and Information Technology, Northwestern Polytechnical University, Xi'an, Shaanxi, 710072, P.R. China (email:ljzong@nwpu.edu.cn).

Fig. 1: A dexterous joint by driving-integrated spherical gears

and have recently attracted increasing interest from robotics communities [6, 7].

Throughout the years, many integrated multi-DoF mechanisms and actuators have been proposed. The traditional mechanism operates by utilizing friction to transfer forces through a sphere and a series of friction wheels placed around it [8–10]. Later, the friction wheels were replaced with omnidirectional wheels [11], providing better flexibility. Nevertheless, slippage is inevitable in such designs, thereby presenting challenges to the progress of associated controls. Another well-known integrated multi-DoF mechanism is the spherical motor, which is an extension of an induction or stepper motor in three dimensions [5, 6]. These designs have the advantage of dexterity and back-drivability. However, the motion range of spherical motors is limited by bearing constraints. The widely recognized wrist mechanism, Omni-Wrist III [12], is also an integrated multi-DoF joint. However, its large size and link interference make it cumbersome and restrict its range of motion. In conclusion, most of the integrated multi-DoF mechanisms still require improvement in terms of compactness, weight, and simplicity.

Spherical gears are a three-dimensional extension of traditional planar gears, providing multiple rotational DoF to change spatial orientation. Due to their high torque transmission and reliable positioning from the teeth, spherical gears have great potential and advantages in realizing multi-DoF single joints [7]. The early proposed spherical gear mechanism consists of two meshing paired spheres, where one sphere has a spherical gear surface with conical-shaped convex teeth, and the corresponding location on the other sphere is a pit of the

same shape. The two spherical gears mesh and transmit power through these convex teeth and pits [13, 14]. Roboticists have subsequently made progressive modifications and refinements to the tooth shape of such gears to improve tooth wear resistance, loading capacity, transmission performance, and other characteristics [15–17]. However, all these spherical gears with discrete teeth do not adhere to the correct transmission principle, resulting in poor transmission performance [18]. In [19], Park et al. proposed the semi-spherical bevel gear, which enables continuous transmission of two spheres in the latitudinal direction. The classical involute gear profile is projected along the longitudinal direction to the poles of the spheres, generating curved teeth uniformly distributed along the spherical surface. The curved teeth provide the ability to mesh continuously along the latitudinal direction. As a result, the formed spherical gear can achieve continuous meshing transmission in the latitudinal direction at any axis intersection angle. On the other hand, Ting et al. proposed the ring-involute spherical gears mechanism in [18] to realize the continuous transmission of two spheres in the longitudinal direction. The involute profile of the same gear is rotationally mapped along the axes of the tooth peaks and valleys, respectively, generating two ring-involute spherical gears conjugate in the longitudinal direction. The two spheres can pure roll in mesh along the longitudinal direction, changing the intersection angle of the polar axes of the two spheres. An interesting product from the industry, Spherigear Transmission [20], shows exciting potential through the spatial gear structure, but unfortunately, it is not globally surface drivable, and external fixed frame limitations lead to its singular transmission. None of the above works have been able to achieve continuous drivable transmission across the entire spherical surface. Furthermore, prior research on spherical gears has solely focused on the passive gear tooth design, without considering their potential as actuators. Tadakuma et al. have dedicated numerous years to the development of spatial gear drive mechanisms [21–24]. Recently, they pioneered a spherical gear actuator ABENICS in [7], which utilizes innovative gears to enable a 3-DoF ball-and-socket joint interaction. Based on nonslip gear meshing, ABENICS provides high-torque transmission and reliable positioning without 3D sensors and is simple to control. However, the coupled tooth shape causes its singularity, and the external holder drive limits its range of motion. Therefore, a spherical gear-based actuator capable of continuous spatial transmission and dexterous joint motion is still under investigation.

The rolling contact joint, a bio-inspired dexterous joint, is formed when one body rolls without slipping over another body [2]. Due to its ability to simplify controller design and expand workspace [25–27], the rolling contact joint holds great promise for developing robotic joint actuators that are free from joint limitations or kinematic singularities [28]. Numerous applications and implementations of rolling contact joints have emerged in the last decade [29–33]. Notably, the traditional planar gear is a classic 1-DoF rolling contact joint [34], while some of the attempts to use spherical gears are essentially a type of passive 2-DoF rolling contact joint [13–15]. However, much of the research on rolling contact joints has been restricted to 1-DoF planar motion joints or passive joints, with only one report of a spatial rolling contact joint actuator. Kim recently proposed a virtual 2-DoF rolling contact joint on their humanoid robot LIMS2, which utilized a bevel gear set with wire coupling to imitate rolling contact motion [28]. This mechanism demonstrates the benefits of 2-DoF rolling contact motion in terms of dexterity and singularity-free operation, but the emulation using gear mechanisms limits the motion range. In general, these works on rolling contact joints have joint limitations or kinematic singularities that detract from the dexterity of rolling contact joints. Developing a dexterous multi-DoF rolling contact joint actuator remains a challenge.

This paper presents a novel driving-integrated spherical gear (DISG) that provides full-range and singularity-free joint motion. The proposed spherical tooth surface combines longitudinal and latitudinal tooth surfaces, which are globally meshed and drivable, enabling continuous rolling between the two spherical gears. The DISG is equipped with an internal integrated actuator consisting of an actively driving magnet and a passively following magnet. The magnetic pair between them allows for arbitrary connection points across the spheres, enabling omnidirectional and full-range motion for the DISG. In this study, we analyze the kinematics of the DISG-based joint, including its workspace and singularities. Our findings suggest that the proposed joint has a full-range workspace and no singularities, with superior motion range compared to existing joints. To validate the DISG design, we developed a prototype and demonstrated the kinematic performance of the DISG-based joint. Additionally, we implemented a 3-DoF independent robotic wrist by connecting an additional revolute joint in tandem. Our comparative analysis demonstrates that the DISG-based joint offers advantages in terms of dexterity, motion range, compactness, and lightweight compared to other joint actuators.

The main contributions of this paper are as follows:

1) A novel spherical gear structure is proposed, which allows for global meshing and drivability, resulting in a robust implementation of spatial rolling contact joints.
2) An internally integrated omnidirectional drive magnet pair is proposed, which, together with the spherical gear structure, forms a driving-integrated spherical gear on which a dexterous joint actuator is implemented.
3) The kinematics of DISG are analyzed, and it is demonstrated that the proposed DISG-based dexterous joint possesses kinematic characteristics such as singularity-free and full-range workspace.
4) A series of experiments is conducted to verify the characteristics of DISG. The comparison results with other joint actuators show that the DISG-based joints offer advantages in terms of dexterity, motion range, compactness, and lightweight.

The rest of the paper is organized as follows. Section II presents the mechanical design of DISG. Section III derives the kinematic model of DISG, and examines its singularities and workspace. Section IV analyzes the force and torque capabilities of DISG. Section V performs a series of experiments on a DISG prototype. Section VI discusses the characteristics

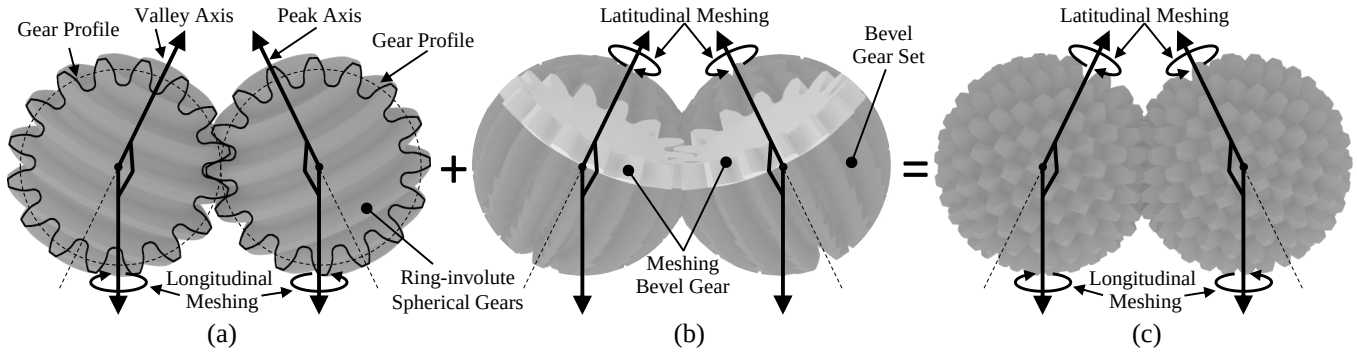

Fig. 2: Two spherical gears meshing along the latitudinal and longitudinal directions respectively are combined to obtain spherical gears meshing along the global sphere. (a) ring-involute spherical gears meshed along the longitude direction; (b) spherical gear pairs meshed along the latitude direction; (c) proposed spherical gears meshed along the global sphere.

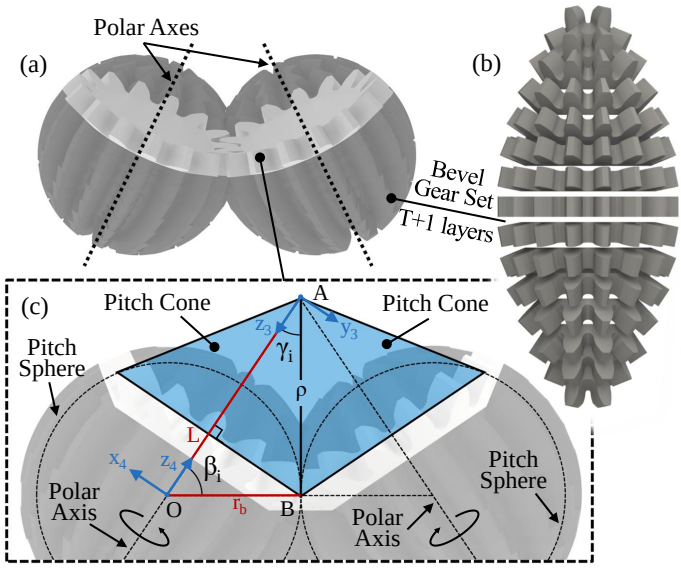

Fig. 3: (a) Improved spherical gears pair meshed along the latitudinal direction; (b) Latitudinal meshing spherical gear can be equated as a superposition of a set of curved bevel gears with equal modulus and varying cross-axis angles; (c) Relative rolling between two spheres can be considered as relative rolling between two pitch cones at corresponding pitch angles.

and manufacturing methods of DISG. Finally, Section VII concludes the entire paper.

II. Mechanical Design

A. Spherical Gear

This paper proposes a method to create tooth profiles for spherical gears that can mesh and drive in both longitudinal and latitudinal directions. This is achieved by combining the tooth profiles of spherical gears that can mesh separately in each direction. Previously, Ting et al. in [18] proposed an involute ring spherical gear that could mesh and roll along the longitudinal direction (Fig. 2(a)). However, this design did not allow for transmission in the latitudinal direction. In contrast, [19] have presented spherical gear pairs that can mesh and roll in the latitudinal direction. We use these spherical gears as references to create our tooth profiles, allowing for meshing in both longitudinal and latitudinal directions(Fig. 2). We start by determining the basic modulus M_B and basic tooth number T_B of the spherical gears based on the desired sphere dimensions. Similar to the concept of pitch circle tangency in planar gears, our proposed spherical gear design features two pitch spheres that are tangent to each other, with the pitch sphere diameter of D_B:

$$D_B = T_B \times M_B. \tag{1}$$

The spherical gears used in combination must be of the same size, sharing the same basic modulus M_B and basic tooth number T_B. It is noteworthy that, akin to their planar counterparts, spherical gears exhibit improved transmission smoothness with an increased tooth number and a reduced modulus. This is attributed to a greater number of teeth being engaged simultaneously, allowing for a more seamless meshing process.

To obtain two conjugate spherical gears pair meshing in the longitudinal direction, we first determine the planar gear profile according to the modulus M_B and tooth number T_B; then rotate the planar gear profile using the axes of the tooth peaks and valleys as the rotation projection axes, respectively. The result of this process is two gears represented as *ring-involute gears (I)* and *ring-involute gears (II)* (Fig. 2(a)), which will be used for the subsequent gear combinations in Fig. 4.

Next we consider the conjugate spherical gears pair meshing in the latitudinal direction. The transmission between bevel gears involves a relative roll between two pitch cones, as depicted in Fig. 3 (c)). Thus, we propose using a combination of curved bevel gears with varying cross-axis angles as spherical gears for latitudinal meshing. This proposed spherical gear is a superposition of a set of bevel gears with varying modulus and varying cross-axis angles. Furthermore, the teeth number of each bevel gear is related to its latitudes. Notably, we employ a bevel gear that permits the cross angle to vary, which was introduced by Park [19]. Its mathematical model can be derived from the traditional bevel gear mathematical model [35] (see Appendix A). In addition, the latitudinal meshing spherical gear is split into a gear set comprising $T_B + 1$ bevel

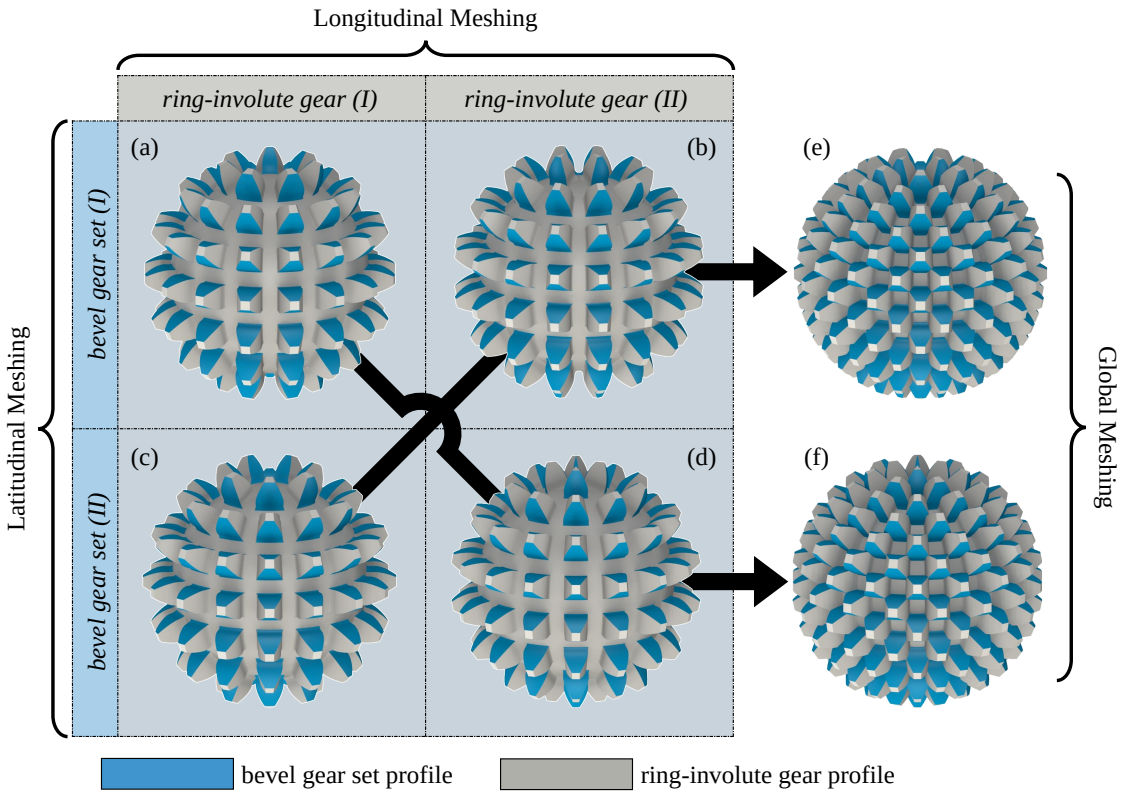

Fig. 4: Two conjugate spherical gear meshes along the both latitudinal and longitudinal directions can be obtained by the intersection and combination of the profiles of ring-involute gears and bevel gear sets.

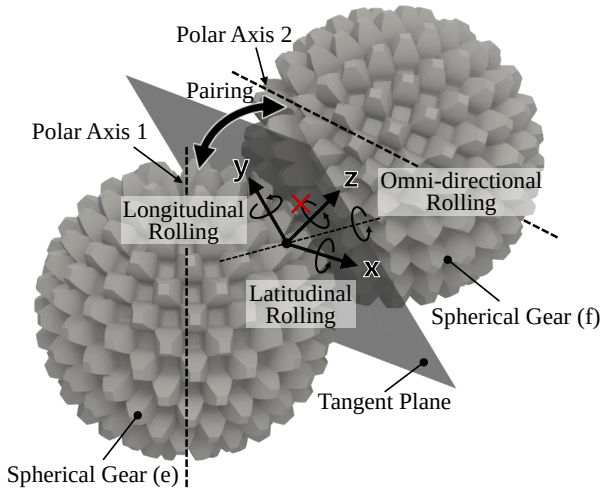

Fig. 5: The relative motion between the proposed spherical gears, where x and y axes of the tangent plane coordinate system (in the tangent plane) represent the axes of the 2-DoF of the spherical gear, and there is no relative motion between the spherical gears along the z-axis (perpendicular to the tangent plane).

gears, given that the teeth number of the ring-involute spherical gear is T_B. Fig. 3(b) shows this bevel gear combination, where the pitch circle diameter D_i of the i-th bevel gear is associated with its latitude:

$$D_i = D_B \times \sin(\beta_i), i \in Z, i \in [1, T_B + 1], \tag{2}$$

where $\beta_i = \frac{180^\circ \times (i-1)}{T_B}$ and β_i characterizes its latitude. In the gear combination, the teeth number T_i of the i-th bevel gear is determined by Eq. (3),

$$T_i = \left[\frac{D_i}{M_B} \right], i \in Z, i \in [1, T_B + 1]. \tag{3}$$

The shape of each bevel gear is determined by several factors, including the number of teeth T_i, modulus M_B, and pitch angle $\gamma_i = 90^\circ - \beta_i$. To produce two latitudinally meshed spherical gears, $T_B + 1$ pairs of bevel gears are integrated, with each pair meshing within its designated latitude. This procedure results in two latitudinally meshed spherical gears (Fig. 2(b)), which are denoted as *bevel gear set (I)* and *bevel gear set (II)*. These gear sets are subsequently utilized in the gear combinations depicted in Fig. 4.

Fig. 4 illustrates a method for combining the profiles of ring-involute gears and bevel gear sets to obtain a tooth shape that allows for meshing and drivability along both latitudinal and longitudinal directions. By intersecting the ring-involute gear pair and the bevel gear combination pair, we obtain four spherical gears labeled (a), (b), (c), and (d). Each tooth in the four spherical gears is formed by combining the tooth surfaces of the ring-involute spherical gears and the bevel gear. Specifically, the tooth profile surface along the longitudinal direction is the ring-involute spherical gears tooth surface,

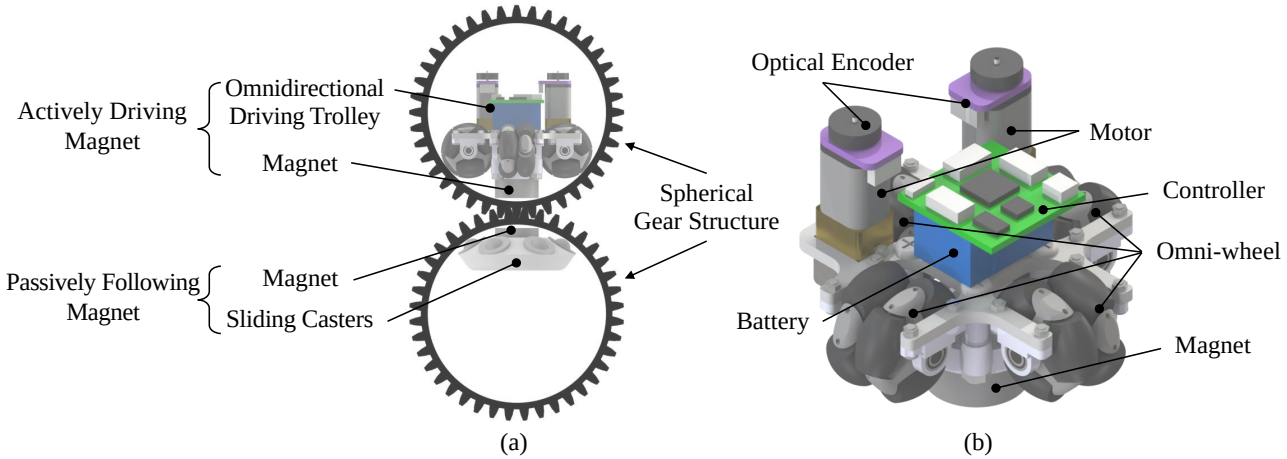

Fig. 6: (a) The proposed omnidirectional internal drive consists of an actively driving magnet and a passively following magnet, where the active-passive magnet pair hold a magnetic connection across the spherical gear surface; (b) The actively driving magnet is an integrated omnidirectional trolley with four omnidirectional wheels and a permanent magnet at the bottom.

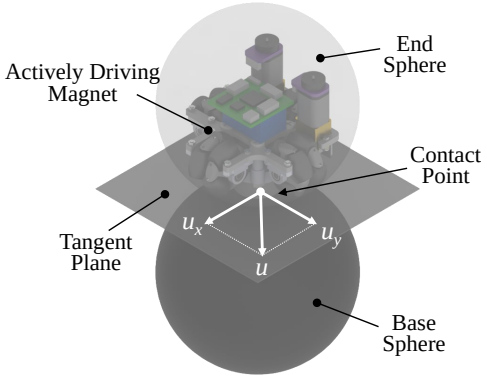

Fig. 7: Omnidirectional internal drives can generate u_x and u_y, and their coupling generates velocities in any direction in the tangential plane, driving the sphere to roll in all directions.

and the latitudinal direction is the bevel gear curved tooth surface. Gears (a) and (b), (c) and (d) mesh in the longitudinal direction, while gears (a) and (c), (b) and (d) mesh in the latitudinal direction. Furthermore, gears (a) and (d), and gears (b) and (c), are non-interfering. Subsequently, the two sets of gears are separately united to obtain two conjugate spherical gears, denoted as (e) and (f), which provide conjugate meshing over the entire sphere.

Next, we discuss the motion between two spherical gears. Fig. 5 illustrates the relative motion between the spherical gears (e) and (f) which are designed for conjugate meshing over the entire sphere. The gears mesh in both longitudinal and latitudinal directions, resulting in available rolls in both directions. By combining the longitudinal and latitudinal rolls, omnidirectional rolling motion can be achieved between the gears. It is important to note that rotation around the vertical axis of the tangent plane is not possible in any attitude due to the constraint of the tooth surface. Furthermore, the relative roll between the two gears can drive the polar axes of the gears in all directions, thus enabling dexterous multi-DoF joint motion.

B. Omni-Driver

The structures of the teeth discussed in Section II-A facilitate an omni-directional rolling motion between two spheres. Furthermore, a mechanism for achieving an omni-directional internal drive is proposed, which together with the proposed spherical gear surface forms DISG, realizing the active multiple-DoF spatial transmission.

The proposed omnidirectional internal drive is depicted in Fig. 6(a) and is comprised of an actively driving magnet and a passively following magnet, which are connected through a magnetic connection across the spherical gear. Fig. 6(b) shows the actively driving magnet, which is an omnidirectional trolley equipped with a permanent magnet at the bottom. The trolley has four omnidirectional wheels that are evenly spaced at 90° intervals, each of which can rotate around and slide laterally along the wheel axis. The four wheels of the omnidirectional trolley are in contact with the sphere, while there is no direct contact between the permanent magnets at the bottom and the sphere shell. The actively driving magnet generates velocities in the tangential plane by two DC motors that drive the two active wheels located 90° apart. The two passive wheels, mounted on the frame with low-friction bearings, serve as supporting casters and rotate passively with the trolley movement. The drive of the two active wheels coupled can generate translational velocities inside the sphere in any direction along the tangential plane, as depicted in Fig. 7. The position and speed of the actively driving magnet inside the sphere can be altered by driving the two motors. Additionally, the actively driving magnet integrates the controller, drive circuit, and battery without any physical connection to the outside, which greatly contributes to the flexible rolling and the expansion of the spherical gear.

The passively following magnet is a permanent magnet that is equipped with six supporting casters capable of sliding in all directions with minimal friction inside the spherical shell. The actively driving magnet and passively following magnet are designed to incorporate two NdFeB permanent

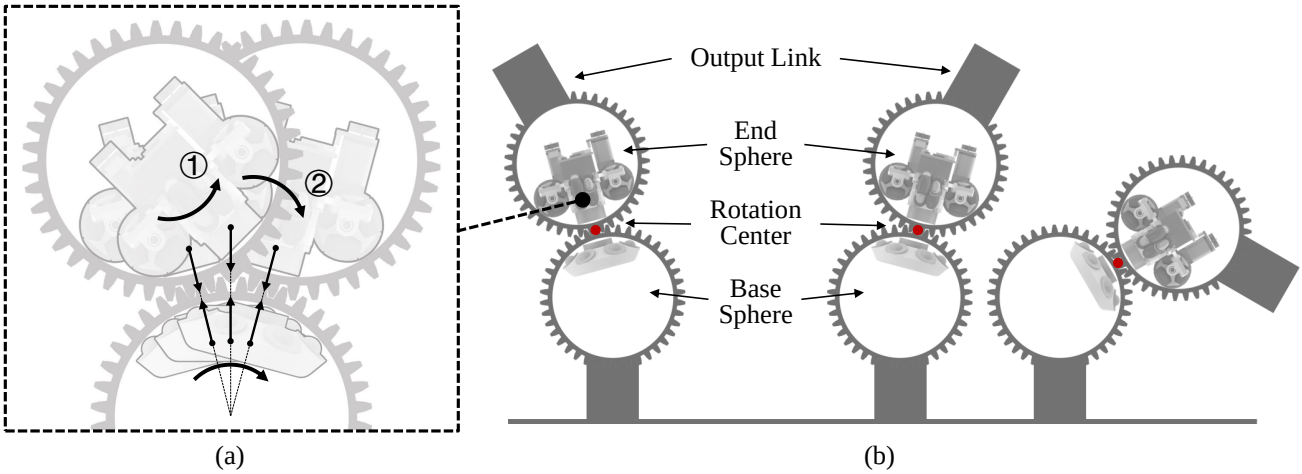

Fig. 8: (a) The dynamic rolling of DISG driven by the active-passive magnet combination. (b) A dexterous multi-DoF rolling contact joint actuator is implemented based on DISG.

magnets with opposite polarity, which generates a strong magnetic force between the two spheres, thus facilitating a robust connection between the two spherical gears. Although the passively following magnet cannot actively move on its own, it can flexibly follow the actively driving magnet due to the magnetic force between them, resulting in low-friction sliding inside the sphere and enabling arbitrary connections between the two spherical gears. It is noteworthy that the force and torque capabilities of the spherical gear pair can be further enhanced by adjusting the size and strength of the passively following magnet.

Fig. 8(a) depicts the spatial transmission of the DISG by means of the actively driving magnet. The DISG relies on DC motors to rotate the friction wheels that move the trolley within the spheres. The relative rolling between the spheres is subsequently propelled by this motion. To ensure efficient transfer of the motor torque through the friction wheel, the friction force between the wheel and the inner wall needs to be substantial throughout the drive process. The joint configuration in the DISG design is dependent on both the load and position of the actively driving magnet. Fig. 8 displays the variation in joint configuration without load, with the magnet co-axial configuration as the static joint configuration(the analysis of the force and moment between the two magnets is shown in Section IV). By driving the actively driving magnet within the sphere, the DISG can shift from one static configuration to the next. The movement of the trolley within the sphere propels the configuration change of the DISG, which occurs in two stages. During the Stage I, the trolley moves actively away from the contact point, while the passively following magnet slides inside the other sphere under magnetic attraction. In the Stage II, the two magnets generate a significant magnetic moment as they move away from the contact point. This moment promotes relative rolling between the spheres until the two magnets reach a stable torque equilibrium state. Generally, the motion of the actively driving magnet within the sphere propels the sliding of the passively following magnet, which generates a torque that propels active rolling between the spheres. The DISG demonstrates good motion capabilities owing to the mobility of the actively driving magnet that can maneuver in all directions within the sphere. This enables one sphere to roll in any direction on the other sphere. The sphere housing the actively driving magnet can traverse along any path and reach any point on the other sphere, thereby facilitating good kinematic performance of the DISG.

In the context of two point-connected bodies, a rolling contact joint is formed when one body rolls without sliding on the surface of the other body [2]. The DISG is comprised of two spherical gears that are interconnected through a magnetic mechanism. Specifically, an actively driving magnet is connected to a passively following magnet across the two gears, which results in a robust point connection between the pitch spheres of the gears. Besides, the meshed tooth shape of the gears ensures that the relative motion between the two spheres is pure rolling, without any sliding motion. As a result of the proposed DISG, a dexterous rolling contact joint actuator is created between the two spherical gears, as illustrated in Fig. 8(b). It is worth noting that traditional implementations of rolling contact joints are restricted to 1-DoF circular rolling contact joints, whereas the DISG-based joint belongs to multi-DoF rolling contact joints. The proposed joint can rotate omnidirectionally in any configuration, while the rotation center varies along the spherical surface according to the joint configuration. This achieves a singularity-free and full-range workspace. A detailed kinematic analysis will be presented in Section III.

III. Kinematics Analysis

In this Section, the kinematics of the DISG-based joint is modeled, i.e., linear and angular velocities of the end body relative to the base body, given the velocity of the omni-drive trolley. Kinematic non-singularity and full-range workspace reachability of the DISG-based joint are proved using the established kinematic equation.

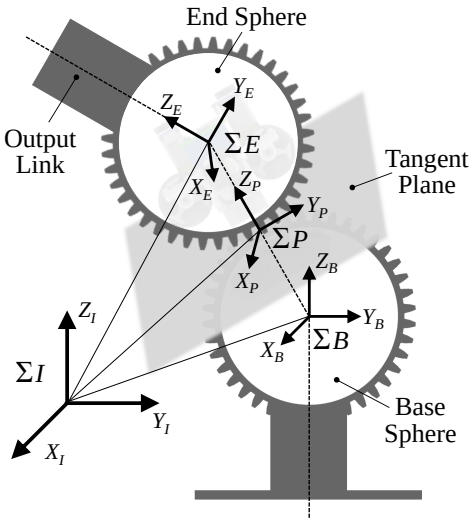

Fig. 9: Related coordinate frames describing the component of the DISG-based joint

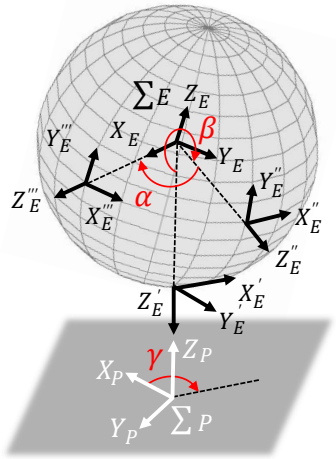

Fig. 10: Euler angles describing the orientation of end sphere E in the DISG-based joint

A. Kinematics Modeling

This Section defines four coordinate frames to represent the objects involved in the DISG-based joint motions, as shown in Fig. 9, including the base body-fixed frame $\sum B$, end body-fixed frame $\sum E$, tangent plane body-fixed frame $\sum P$, and inertial frame $\sum I$.

Defining the DISG-based joint velocity ${}^{B}_{P}\boldsymbol{\omega}_{E}$, which represents the angular velocity of $\sum E$ with respect to $\sum B$ and expressed in the frame $\sum P$ (note that the joint axes are aligned with the axes of the frame $\sum P$). The left superscript '$*$' and subscript '$\#$' represent that a vector is with respect to frame '$\#$' and expressed in frame '$*$'. How the DISG-based joint velocity ${}^{B}_{P}\boldsymbol{\omega}_{E}$ generates linear and angular velocity of $\sum E$ relative to $\sum B$ is the focus of this subsection. A more physically meaningful set of angular velocities ${}^{P}_{P}\boldsymbol{\omega}_{E}$ that closely relate to the omni-driving unit of DISG, as shown in Eq. (5), is defined, it has the following relationship with the DISG-based rolling contact joint velocity ${}^{B}_{P}\boldsymbol{\omega}_{E}$:

$$ {}^{B}_{P}\boldsymbol{\omega}_{E} = {}^{B}_{P}\boldsymbol{\omega}_{P} + {}^{P}_{P}\boldsymbol{\omega}_{E} = 2\,{}^{P}_{P}\boldsymbol{\omega}_{E}, \tag{4} $$

The velocity of the omni-drive trolley are defined easily in the tangent plane $\sum P$ as u_x and u_y, which are used to realize the DISG-based joint velocity and satisfy the relationships with ${}^{P}_{P}\boldsymbol{\omega}_{E}$:

$$ \begin{cases} u_x - l\,{}^{P}_{P}\omega_{Ey} = 0, \\ u_y + l\,{}^{P}_{P}\omega_{Ex} = 0, \\ {}^{P}_{P}\omega_{Ez} = 0, \end{cases} \tag{5} $$

due to the *pure meshing rolling* assumption of the motions between the base and end bodies, where l is the radius of the sphere bodies. It is worth noting that rotations of two bodies around the vertical axis of their tangent plane is not allowed due to rotational torsion.

This paper uses Euler angles to describe the orientation of the end body $\sum E$ with respect to the tangent plane $\sum P$, as shown in Fig. 10, including the azimuth α and elevation β of the contact point between the end-sphere and tangent plane, and the holonomy angle γ between the x-axis of the $\sum P$ and Gaussian frame[26] at the contact point. As a result, the coordinate transformation matrix from $\sum E$ to $\sum P$ can be expressed as

$$ {}^{P}\boldsymbol{R}_{E} = \boldsymbol{R}_{x}(\pi)\,\boldsymbol{R}_{z}(\gamma)\,\boldsymbol{R}_{x}(\beta)\,\boldsymbol{R}_{y}(-\alpha), \tag{6} $$

where $\boldsymbol{R}_x, \boldsymbol{R}_y, \boldsymbol{R}_z$ are elementary rotations [2].

The derivatives of the Euler angles (α, β, γ) and the angular velocity of the end body relative to tangent plane ${}^{P}_{P}\boldsymbol{\omega}_{E}$ satisfy the relation:

$$ {}^{P}_{P}\boldsymbol{\omega}_{E} = \boldsymbol{J}_{A}\left(\frac{\mathrm{d}}{\mathrm{d}t}\begin{bmatrix}\alpha & \beta & \gamma\end{bmatrix}^{\top}\right) \tag{7} $$

with the Jacobian matrix $\boldsymbol{J}_A$

$$ \begin{aligned} \boldsymbol{J}_{A} &= \left[-{}^{P}\boldsymbol{R}_{M}\boldsymbol{j} \,|\, \boldsymbol{R}_{x}(\pi)\,\boldsymbol{R}_{z}(\gamma)\,\boldsymbol{R}_{x}(\beta)\boldsymbol{i} \,|\, \boldsymbol{R}_{x}(\pi)\,\boldsymbol{R}_{z}(\gamma)\boldsymbol{k}\right] \\ &= \begin{bmatrix} \mathrm{c}\beta\,\mathrm{s}\gamma & \mathrm{c}\gamma & 0 \\ \mathrm{c}\beta\,\mathrm{c}\gamma & -\mathrm{s}\gamma & 0 \\ \mathrm{s}\beta & 0 & -1 \end{bmatrix}, \end{aligned} \tag{8} $$

where $\mathrm{c}(\cdot)$ and $\mathrm{s}(\cdot)$ are short for $\cos(\cdot)$ and $\sin(\cdot)$, respectively, and reversely

$$ \frac{\mathrm{d}}{\mathrm{d}t}\begin{bmatrix}\alpha \\ \beta \\ \gamma\end{bmatrix} = \begin{bmatrix} \frac{\mathrm{s}\gamma}{\mathrm{c}\beta} & \frac{\mathrm{c}\gamma}{\mathrm{c}\beta} & 0 \\ \mathrm{c}\gamma & -\mathrm{s}\gamma & 0 \\ \frac{\mathrm{s}\beta\,\mathrm{s}\gamma}{\mathrm{c}\beta} & \frac{\mathrm{s}\beta\,\mathrm{c}\gamma}{\mathrm{c}\beta} & -1 \end{bmatrix}\begin{bmatrix} {}^{P}_{P}\boldsymbol{\omega}_{Ex} \\ {}^{P}_{P}\boldsymbol{\omega}_{Ey} \\ {}^{P}_{P}\boldsymbol{\omega}_{Ez} \end{bmatrix}, \tag{9} $$

Using the non-holonomic constraints in Eq. (5), Eq. (9) turns into

$$ \frac{\mathrm{d}}{\mathrm{d}t}\begin{bmatrix}\alpha \\ \beta \\ \gamma\end{bmatrix} = \begin{bmatrix} \frac{\mathrm{c}\gamma}{l\cdot\mathrm{c}\beta} & -\frac{\mathrm{s}\gamma}{l\cdot\mathrm{c}\beta} \\ -\frac{\mathrm{s}\gamma}{l} & -\frac{\mathrm{c}\gamma}{l} \\ \frac{\mathrm{s}\beta\,\mathrm{c}\gamma}{l\cdot\mathrm{c}\beta} & -\frac{\mathrm{s}\beta\,\mathrm{s}\gamma}{l\cdot\mathrm{c}\beta} \end{bmatrix}\begin{bmatrix} u_x \\ u_y \end{bmatrix}. \tag{10} $$

When omni-drive trolley moves with the velocity u_x and u_y, the update of the Euler angles α, β, γ and the corresponding ${}^{P}\boldsymbol{R}_{E}$ shown in Eq. (6) follows the law in Eq. (10). Assuming without loss of generality that the coordinate frames $\sum B, \sum P$ and $\sum E$ are aligned at the initial moment, then ${}^{B}\boldsymbol{R}_{P} = {}^{P}\boldsymbol{R}_{E}$ and is obtained in Eq. (6).

Defining the radius of the sphere bodies as l, therefore, the position of the end body $\sum E$ relative to the base body $\sum B$ can be calculated as follows:

$$ {}^{B}_{B}\boldsymbol{r}_{E} = {}^{B}\boldsymbol{R}_{P}\left(2l\ {}^{P}_{P}\hat{\boldsymbol{z}}\right), \tag{11} $$

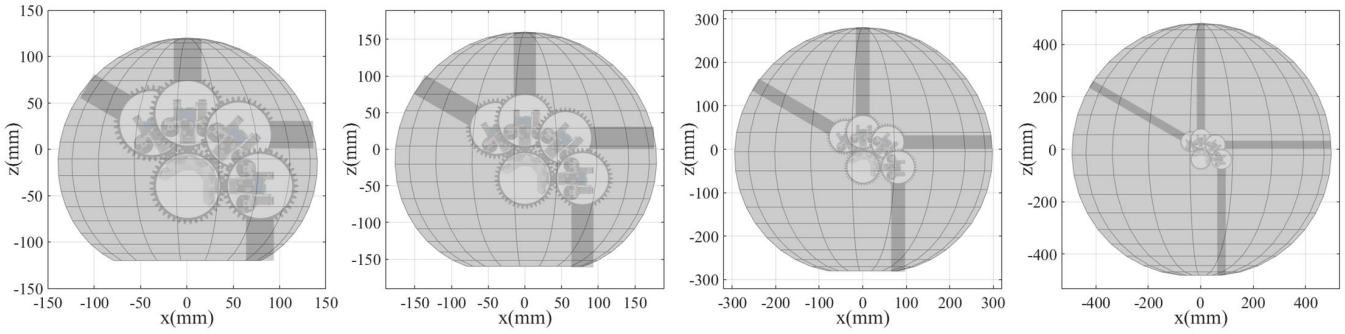

Fig. 11: The workspace of the DISG-based joint end for $\frac{l_o}{R} =$ (a)1, (b)2, (c)5, (d)10

where ${}^{P}_{P}\hat{\boldsymbol{z}} = [0, 0, 1]^{\top}$ is the expression of a unit vector along z-axis of $\sum P$.

Having the non-holonomic constraints Eq. (5), the angular velocity of $\sum E$ relative to $\sum B$ is

$$\begin{aligned} {}^{B}_{B}\boldsymbol{\omega}_{E} &= {}^{B}_{B}\boldsymbol{\omega}_{P} + {}^{P}_{B}\boldsymbol{\omega}_{E} \\ &= -{}^{P}_{B}\boldsymbol{\omega}_{B} + {}^{P}_{B}\boldsymbol{\omega}_{E} \\ &= -{}^{B}\boldsymbol{R}_{P}\,{}^{P}_{P}\boldsymbol{\omega}_{B} + {}^{B}\boldsymbol{R}_{P}\,{}^{P}_{P}\boldsymbol{\omega}_{E} \\ &= 2\,{}^{B}\boldsymbol{R}_{P}\,{}^{P}_{P}\boldsymbol{\omega}_{E} \\ &= \boldsymbol{J}_{\boldsymbol{\omega}}\begin{bmatrix} u_x & u_y \end{bmatrix}^{\top}, \end{aligned} \tag{12}$$

when omni-drive trolley moves with the velocity u_x and u_y, and the angular Jacobian matrix $\boldsymbol{J}_{\boldsymbol{\omega}}$ is calculated as

$$\boldsymbol{J}_{\boldsymbol{\omega}} = 2\,{}^{B}\boldsymbol{R}_{P}\begin{bmatrix} 0 & -\frac{1}{l} \\ \frac{1}{l} & 0 \\ 0 & 0 \end{bmatrix}, \tag{13}$$

using the non-holonomic constraints Eq. (5).

The linear velocity of $\sum E$ relative to $\sum B$, when omni-drive trolley moves with the velocity u_x and u_y, is obtained by deriving the Eq. (11):

$$\begin{aligned} {}^{B}_{B}\boldsymbol{v}_{E} &= 2\,l\left[{}^{B}_{B}\boldsymbol{\omega}_{P}\right]_{\times}{}^{B}\boldsymbol{R}_{P}\,{}^{P}_{P}\hat{\boldsymbol{z}} \\ &= -2\,l\left[{}^{B}\boldsymbol{R}_{P}\,{}^{P}_{P}\hat{\boldsymbol{z}}\right]_{\times}{}^{B}_{B}\boldsymbol{\omega}_{P} \\ &= -l\left[{}^{B}\boldsymbol{R}_{P}\,{}^{P}_{P}\hat{\boldsymbol{z}}\right]_{\times}\boldsymbol{J}_{\boldsymbol{\omega}}\begin{bmatrix} u_x & u_y \end{bmatrix}^{\top} \\ &= \boldsymbol{J}_{\boldsymbol{v}}\begin{bmatrix} u_x & u_y \end{bmatrix}^{\top}, \end{aligned} \tag{14}$$

where the symbol '$\times$' represents the skew-symmetric matrix of a vector, and the linear Jacobian matrix $\boldsymbol{J}_{\boldsymbol{v}}$ is calculated as

$$\boldsymbol{J}_{\boldsymbol{v}} = -l\left[{}^{B}\boldsymbol{R}_{P}\,{}^{P}_{P}\hat{\boldsymbol{z}}\right]_{\times}\boldsymbol{J}_{\boldsymbol{\omega}}. \tag{15}$$

B. Singularity Analysis

The kinematic singularity of the DISG-based joint is examined through the established kinematic model. In this context, singularities refer to joint configurations where the motion of the joint cannot be generated in a certain direction despite the provision of high velocities to the omni-drive wheels.

In mathematical sense, the nonsingular orientations of the DISG-based joint are those orientations for which there is at least one set of wheel velocities (u_x, u_y) capable of generating the desired joint velocity. This indicates that the mapping matrix from wheel velocity to joint velocity is a matrix of full rank for all feasible joint configurations within the workspace, which could be validated in a straightforward way by calculating that the determinant of the mapping matrix is not zero.

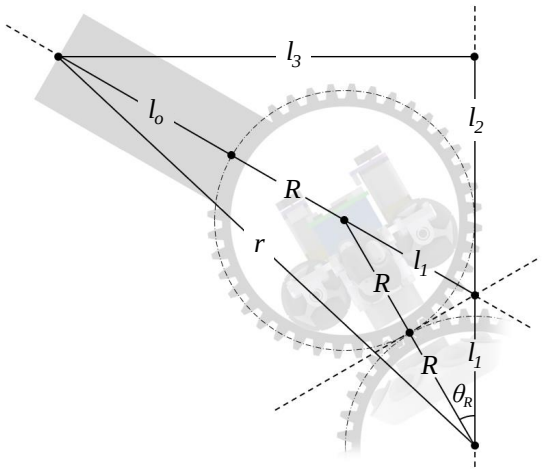

Fig. 12: The geometric parameter of the DISG-based joint.

Recalling the DISG-based joint velocity ${}^{B}_{P}\omega_{E}$ defined in the Section III-A and its relationship with the omni-wheel velocity in non-holonomic constraints (5), a compact mapping from the omni-wheel velocity to DISG-based joint velocity can be formulated as

$$\begin{bmatrix} {}^{B}_{P}\boldsymbol{\omega}_{Ex} \\ {}^{B}_{P}\boldsymbol{\omega}_{Ey} \end{bmatrix} = \boldsymbol{Q}\begin{bmatrix} u_x \\ u_y \end{bmatrix}, \tag{16}$$

where

$$\boldsymbol{Q} = \begin{bmatrix} 0 & -\frac{2}{l} \\ \frac{2}{l} & 0 \end{bmatrix} \tag{17}$$

is the mapping matrix from the wheel velocity to the joint velocity.

It is readily to calculate the determinant of $\boldsymbol{Q}$ as

$$\mathrm{Det}(\boldsymbol{Q}) = \frac{4}{l^2} \neq 0. \tag{18}$$

Henceforth, it can be inferred that the mapping matrix between the wheel velocity and the joint velocity is consistently of full rank. This observation indicates that the DISG-based joint proposed is free from kinematic singularities throughout its workspace.

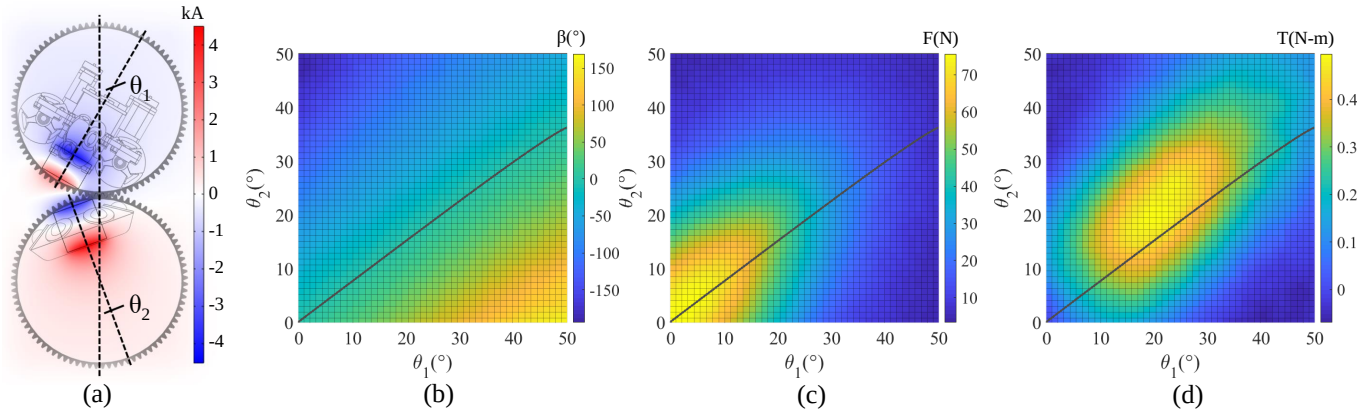

Fig. 13: Strength analysis of DISG: (a) Magnetic field distribution between two magnets inside the spherical gears; (b), (c) and (d) show the clamping angle β, the magnitude of the magnetic force F_m, and the torque at the contact point T_B, relative to θ_1 and θ_2, respectively.

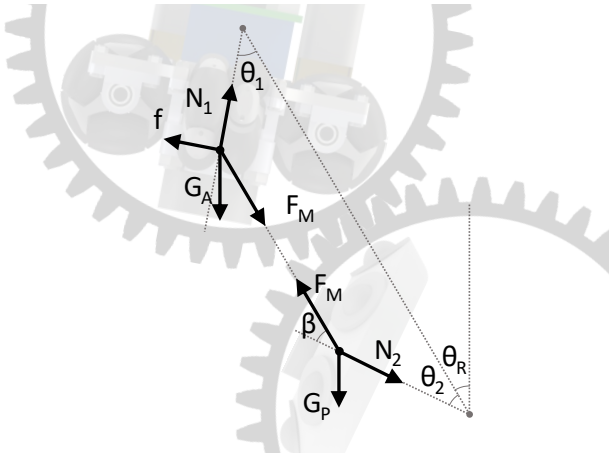

Fig. 14: The force analysis of the active and passive magnets in DISG.

C. Workspace Analysis

This section analyzes the workspace of the DISG-based joint. In Fig. 12, the geometric parameters of the DISG-based joint end are presented. Based on the analyzed geometry, it can be inferred that

$$\begin{cases} l_1 \cos\theta_R = R \\ (l_1 + l_o + R)\cos 2\theta_R = l_2 \\ (l_1 + l_o + R)\sin 2\theta_R = l_3 \end{cases}. \tag{19}$$

The distance r between the end of the output link and the origin of $\sum B$ is solved as

$$\begin{aligned} r &= \sqrt{(l_1 + l_2)^2 + l_3^2} \\ &= \sqrt{l_1^2 + l_2^2 + l_3^2 + 2l_1 l_2} \\ &= \sqrt{4R^2 + (l_o + R)^2 + 4R(l_o + R)\cos\theta_R} \end{aligned}, \tag{20}$$

where θ_R is the angle between the line connecting the two spheres and the vertical direction, characterizing the configuration of the DISG-based joint, R is the radius of the sphere, and l_o is the length of the output link. Based on Eq. (19), it is evident that in a DISG-based joint with fixed parameters (i.e., given values of R and l_o), the distance r changes as a function of θ_R. This is a consequence of the fact that the rotation center of the DISG-based joint is the point of contact between the two spheres, and it varies continuously with the configuration of the joint. Rolling contact motion involves a motion in which the rotation center varies along the surface of the base sphere $\sum B$, and as such, the joint configuration has an impact on the distance between the end sphere $\sum E$ and the base sphere $\sum B$.

Fig. 11(a)-(d) depict the workspace of DISG-based joint ends for various l_o-to-R ratios. It is noteworthy that the motion is non-singular, and the complete 3-D workspace can be obtained by rotating the plot 360° around the z-axis. We present the cross-section to facilitate a clear comprehension of the relationship between the shape and the workspace boundary. Evidently, the joint exhibits a full range of motion, and as the l_o-to-R ratio increases, the workspace approaches a standard sphere. According to Eq. (20), $r \approx l_o$ when $l_o \gg R$, implying that the distance between the end and the base $\sum B$ is approximately equal to the length of the output link. Hence, the workspace of the DISG-based joint can be approximated as a standard sphere, rendering the joint a spherical joint in such a scenario. In conclusion, the proposed DISG-based joint is a 2-DoF full-range joint, whose workspace approximates a sphere.

IV. Forces and Torques in DISG

This section presents an analysis of the strength of the DISG, specifically examining its breaking force and output torque. The forces and drives in the DISG system stem primarily from the magnets used. Therefore, this analysis first considers the forces and torques between the magnets themselves. In the DISG, two permanent magnets are separated by spheres and maintained in a connected state through magnetic attraction. The magnetic force and torque between the two permanent magnets are dependent on the poses of the magnets within the spheres, which, in turn, are influenced by the geometrical parameters of the magnets, including their size, material, and geometric constraints imposed by the DISG

system. To investigate the relationship between the magnetic force and torque and these parameters, a series of finite element method (FEM) calculations were performed under conditions consistent with a manufactured prototype of the DISG system. This prototype includes a $10 \times 10 \times 10\,\text{mm}^3$ actively driving cylindrical magnet, a $10 \times 10 \times 20\,\text{mm}^3$ passively following cylindrical magnet, and a spherical gear surface made of resin with a tangential pitch sphere diameter of 86 mm and an inner diameter of 84 mm (detailed in Table I). Fig. 13(a) shows the magnetic field distribution between the two cylindrical magnets inside the spherical gear, where θ_1 and θ_2 denote the angles between the central axes of the magnets and the line connecting the spherical center, respectively. Fig. 13(c) and (d) illustrate the magnitude of the magnetic force connecting the two magnets and the torque at the contact point, respectively, with respect to θ_1 and θ_2. As shown in Fig. 13(c), the magnetic force decreases monotonically as either θ_1 or θ_2 increases. At $\theta_1 = \theta_2 = 0°$, the magnetic force is maximal at 75.8 N, indicating that the force is strongest when the two magnets are coaxial. The torque between the magnets, depicted in Fig. 13(d), increases as θ_1 and θ_2 increase from 0 and reaches a maximum value of 0.49 N · m at $\theta_1 = \theta_2 = 21°$. Notably, the strength and size of the active-passive magnet pairing can be increased to enhance the magnetic force and torque between them.

Furthermore, the internal state of the trolley and the joint configuration have a combined effect on the connection force and output torque of the spherical gear. Therefore, we proceed to examine the force of DISG during driving. As detailed in Section II-B, the trolley moves under active control and attracts the following magnet to passively follow. Subsequently, the magnetic torque produced drives DISG to rotate. The output torque of DISG, which is related to θ_1 and θ_2, is the magnetic torque between the misaligned magnet pairs. Fig. 13(c) and (d) display the magnetic force and torque for any given θ_1 and θ_2. However, many of these states are not feasible as, in reality, θ_2 simply follows the changes in θ_1 passively, indicating that θ_2 is determined by θ_1. For instance, let us consider the case of no load, where we can investigate how θ_2 changes passively when θ_1 changes actively. In Fig. 14, we can see the situation where the actively driving magnet leads the passively following magnet to slide. By analyzing the forces acting on the passively following magnet in this scenario, we have

$$F_M \sin(\beta) = G_P \sin(\theta_2 + \theta_R), \tag{21}$$

where F_M , β are associated with θ_1 and θ_2. To put it simply, given a magnet weight G_P and joint angle θ_R, we can express Eq. (21) as a binary equation of θ_1 and θ_2, which means we can view θ_2 as a function of θ_1. Using this, we can then determine the connection force and output torque. To obtain the maximum DISG strength, we block the rotation and ignore the weight of the passive magnet, i.e., $G_P = 0$ and θ_R is fixed. By utilizing the interpolation method, we can obtain the three functions of F_M, β, and T based on the data in Fig. 13(b), (c), and (d),

$$\beta = f_\beta(\theta_1, \theta_2), \tag{22}$$

$$F_M = f_{F_M}(\theta_1, \theta_2), \tag{23}$$

$$T = f_T(\theta_1, \theta_2). \tag{24}$$

Then we substitute Eq. (23) and (22) into the Eq. (21) to get θ_2 as a numerical function about θ_1,

$$\theta_2 = f_{\theta_2}(\theta_1), \tag{25}$$

as shown in the black line in Fig. 13(b). We can observe that θ_2 increases in an almost linear fashion as θ_1 increases. Moreover, by substituting Eq. (25) into Eqs. (23) and (24), we can calculate the magnetic force and torque with respect to θ_1. In Fig. 13(c) and (d), we have also plotted Eq. (25) which depicts the magnetic force F_m and torque T_B as a function of θ_1 along the black lines. As shown in Fig. 13(c), the magnetic force at $\theta_1 = 0°$ is the highest, with a value of 75.8 N, but it decreases consistently as θ_1 increases, dropping rapidly to 5.4 N at $\theta_1 = 50°$. Similarly, Fig. 13(d) demonstrates that the magnetic torque between the spheres increases initially and then decreases as θ_1 rises, reaching a maximum value of 0.43 N · m at $\theta_1 = 20.7°$. Hence, the DISG's theoretical breaking force is 75.8 N, while the maximum output torque is 0.43 N·m. It is worth noting that as illustrated in Fig. 13(c), the magnetic connection force between the spheres decreases continuously as θ_1 increases. This implies that continuous driving of the trolley when the DISG is blocked may result in a reduction of DISG strength or even breakage. The actual measurement results of the prototype indicate that the maximum connection force and output torques are 72.5 N and 0.39 N·m, respectively, which are consistent with our analysis results.

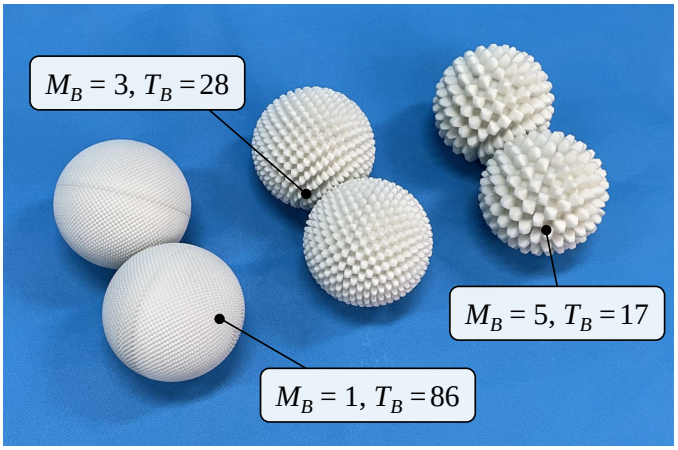

Fig. 15: The DISG prototypes with different modulus

V. Experiments and Results

This section demonstrates the spherical gear prototype and its capability for global and unlimited meshing through experimentation. Moreover, we expound upon the inherent kinematic characteristics of the DISG-based joint, including singularity-free motion and a full-range workspace. The verification of the derived kinematic model is also outlined. The inclusion of a loaded DISG control experiment further enhances the presentation. Additionally, we introduce a 3-DoF independent full-range wrist extension based on DISG and conduct comparative analyses with analogous joint configurations.

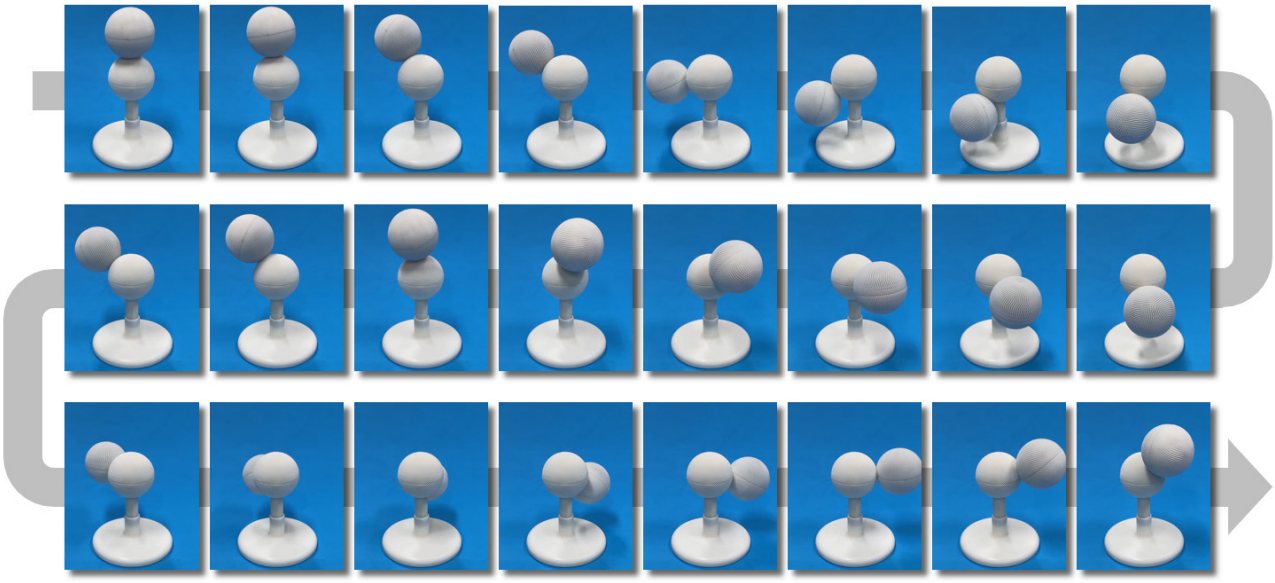

Fig. 16: A spherical gear rolls on the surface of another with an ∞-shape trajectory.

A. Global meshing spherical gears

Fig. 15 illustrates a variety of spherical gear prototypes, each possessing distinct modulus and tooth numbers while sharing similar pitch sphere diameters. Similar to planar gears, spherical gears exhibit enhanced smoothness in operation as the tooth number increases, facilitating improved gear functionality. However, caution is needed as overly large gear modulus increases magnet pair distance, harming DISG strength and performance. Furthermore, the sphere housing the mechanism must be adequately sized to comfortably contain the trolley; otherwise, an appropriate fit cannot be achieved. Taking these factors into consideration, we opt to employ gear parameters of $M_B = 1$ and $T_B = 86$ for our subsequent experimental endeavors.

To validate the ability of the two spherical gears to mesh globally and without restriction, we designed a large range of motion trajectory that would cover as much of the sphere as possible. The experimental setup involved fixing one spherical gear to the base, and then using an active-passive magnet combination to connect the two gears. The DISG prototype was set to follow an ∞-shaped rolling trajectory driven by the actively driving magnet. Fig. 16 displays some key frames captured during the desired trajectory performed by the spherical gear pair, demonstrating the nature of the global drivable meshing and the unlimited rolling of the spherical gear pair.

B. DISG-based rolling contact joint

Fig. 17 depicts a DISG-based rolling contact joint prototype with gear parameters matching those in Section V-A. The gear housing's dimensions are specified: a pitch sphere diameter of 86 mm and inner sphere diameter of 84 mm. Utilizing N52 NdFeB magnets, a $10 \times 10 \times 20\,\mathrm{mm}^3$ cylindrical magnet is affixed to the actively driving magnet, and a $10 \times 10 \times 10\,\mathrm{mm}^3$ cylindrical magnet is affixed to the passively following magnet.

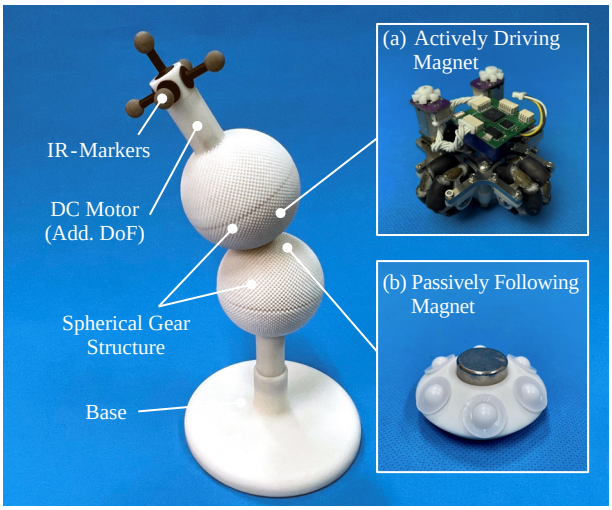

Fig. 17: Prototype of the DISG-based rolling contact joint

The magnet pair offers a max connection strength of 72.5 N and a max load moment of 0.39 N $\cdot$ m. Additionally, a DC motor is incorporated into the output link of the joint as an extra DoF to form the joint combination in the RC-R configuration. In Section V-D, we will demonstrate the kinematic performance of a 3-DoF independent robotic wrist extension using this additional revolute joint. The end of the joint output link is equipped with a tracking marker consisting of five infrared reflection markers (IR-markers). The position and attitude of the joint end can be obtained using the motion capture system. Table I provides the detailed parameters of the DISG-based rolling contact joint.

The DISG-based joint kinematics were validated through prototype experiments and the dexterity of the DISG-based rolling contact joint was demonstrated. Fig. 18 depicts the joint configuration characterization, where a 2-DoF DISG-based joint can be oriented solely with the azimuth ψ and the evaluation θ. Notably, an intriguing aspect of the configuration

TABLE I: DISG PROTOTYPE PARAMETERS

Characteristics		**Values**
Actively Driving Magnet	Mass	115.4 g
	Magnet Size	$10\times10\times10$ mm^3
	(BH)max	52MGOe
Passively Following Magnet	Mass	82.5 g
	Magnet Size	$10\times10\times20$ mm^3
	(BH)max	52MGOe
Spherical Gear Structure	T_B	86
	M_B	1
	Pitch Sph. Diam.	86 mm
	Int. Sph. Diam.	84 mm
Max. Breaking Force		72.5 N
Max. Output Torque		0.39 N · m

characterization is that our methodology can characterize the entire 2-DoF space, but it becomes redundant at the poles. Specifically, when $\theta = 0$, the output linkage is consistently oriented in a vertical upward direction, regardless of the ψ value, thereby rendering ψ redundant when expressing the orientation at the poles. As a result, when the DISG configuration shifts in the vicinity of the poles, ψ undergoes significant changes. The optical encoders mounted on the wheels provide actual position feedback for the actively driving magnet (c_{1a}, c_{2a}), while the kinematic model calculates the target encoder counts (c_{1t}, c_{2t}) corresponding to the desired joint configurations (ψ_t, θ_t). A closed-loop position control approach is adopted using a PID controller based on the target input from the kinematics (c_{1t}, c_{2t}) and the actual position feedback from the encoder (c_{1a}, c_{2a}), and the PWM output is directly applied to drive the two DC motors of the actively driving magnet. The motion capture system is used to measure the end's attitude. Several reference configurations are assigned, they are: $C_1[-180, 90]^\circ$, $C_2[-135, 90]^\circ$, $C_3[30, 90]^\circ$, $C_4[-45, 135]^\circ$, and $C_5[0, 180]^\circ$, which are executed sequentially with a stopping time of 2 seconds each. Since this experiment is essentially an open-loop control based on the kinematic model, the accuracy of reaching the target configuration is heavily dependent on the correctness of the kinematic model.

Fig. 19 illustrates various motion frames captured at key moments, along with the orientation of the end during the prototype's sequential passage through the reference configurations. In Fig. 19(b), the Euler angles measured by motion capture and those calculated based on the encoder measurements and kinematics model are presented. The motion trajectory showcases the large workspace of the DISG-based joint. In the experiment depicted in Fig. 19, the measured trajectory and the kinematics-based calculations closely overlap throughout the motion, where the attitude errors of the end in each reference configuration are $e_1[+1.41, -1.65]^\circ$, $e_2[+1.89, -1.92]^\circ$, $e_3[+1.23, -3.18]^\circ$, $e_4[+1.87, -3.64]^\circ$ and $e_5[-3.75, -1.16]^\circ$ respectively. The subplots demonstrate that the maximum errors for both Euler angles are less than 4° , confirming the accuracy of the derived kinematic model. Regarding experimental errors, the precision of position control

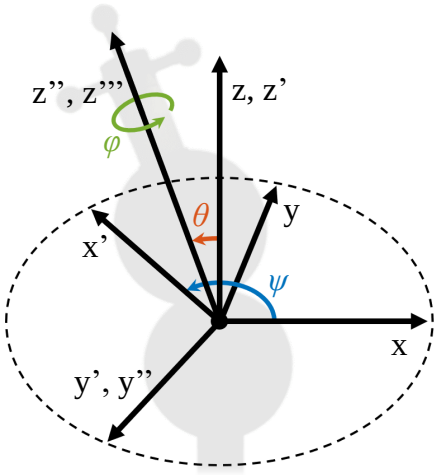

Fig. 18: The joint configuration is characterized by azimuth ψ , evaluation θ, and yaw ϕ.

is impacted by both the gravity and the wheel slippage. The effect of gravity on the positioning error is negligible since there is no additional load. However, wheel slippage is the primary factor contributing to the error observed in Fig. 19(b). The DISG drive employs DC motors to rotate the wheel and transmit torque via the friction wheel to move the trolley in the sphere. Due to manufacturing process limitations, slight and uncontrollable slippage occurs on the friction wheel, causing the motor encoder measurements to inaccurately calculate the trolley's position inside the sphere as it moves through it. Although these errors are minor, the cumulative errors resulting from long working hours are not negligible and are the primary reason for position errors in the experimental results.

C. Singularity-free nature of DISG-based joint

This section presents a comparison between the proposed DISG-based robotic wrist and a traditional 2-DoF wrist, composed of two revolute joints in series. Our aim is to demonstrate the singularity-free nature of the proposed joint. Both wrists can be described using the azimuth ψ and the elevation θ, as depicted in Fig. 19(a). The conventional 2-DoF wrist experiences singularity at $\theta = 0^\circ$, causing a loss of velocity along the second revolute joint axis. Conversely, the proposed DISG-based joint can rotate freely in all directions within the workspace, without encountering any singularities.

To conduct the comparison, we set identical joint angular velocities and motion trajectories for both wrists. Specifically, we specified the initial configuration $[90, 90]^\circ$, the intermediate configuration $[0, 0]^\circ$, and the final configuration $[0, 90]^\circ$. Fig. 20(a) presents motion frames captured at different time intervals during the tracking of the desired trajectory by both wrists, while Fig. 20(b) displays the corresponding changes in Euler angles. Notably, the conventional wrist reaches singularity at $\theta = 0^\circ$, requiring it to adjust the azimuth ψ before continuing from the intermediate to the final configuration. In contrast, the proposed DISG-based joint can can move directly through the desired trajectory, illustrating its singularity-free nature.

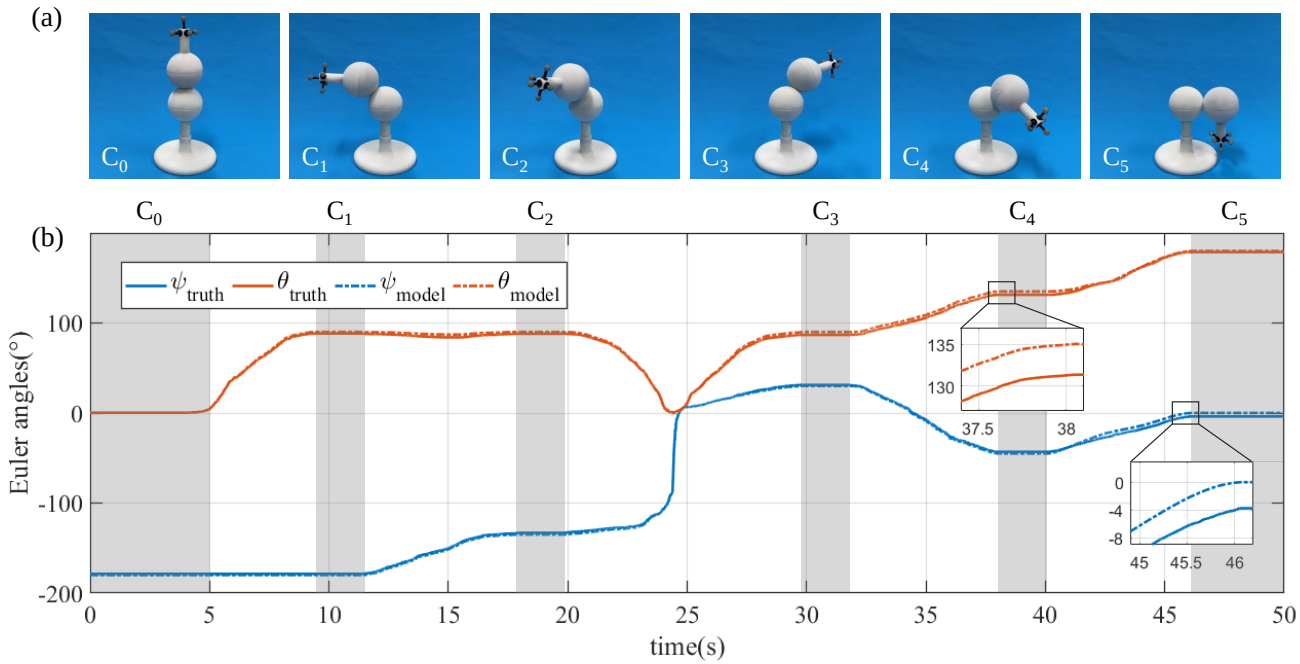

Fig. 19: The kinematics of the 2-DoF DISG-based joint is verified by prototype experiments: during the DISG-based joint sequence through the reference configuration, (a) some motion frames captured at key moments, and (b) euler angles characterizing orientation.

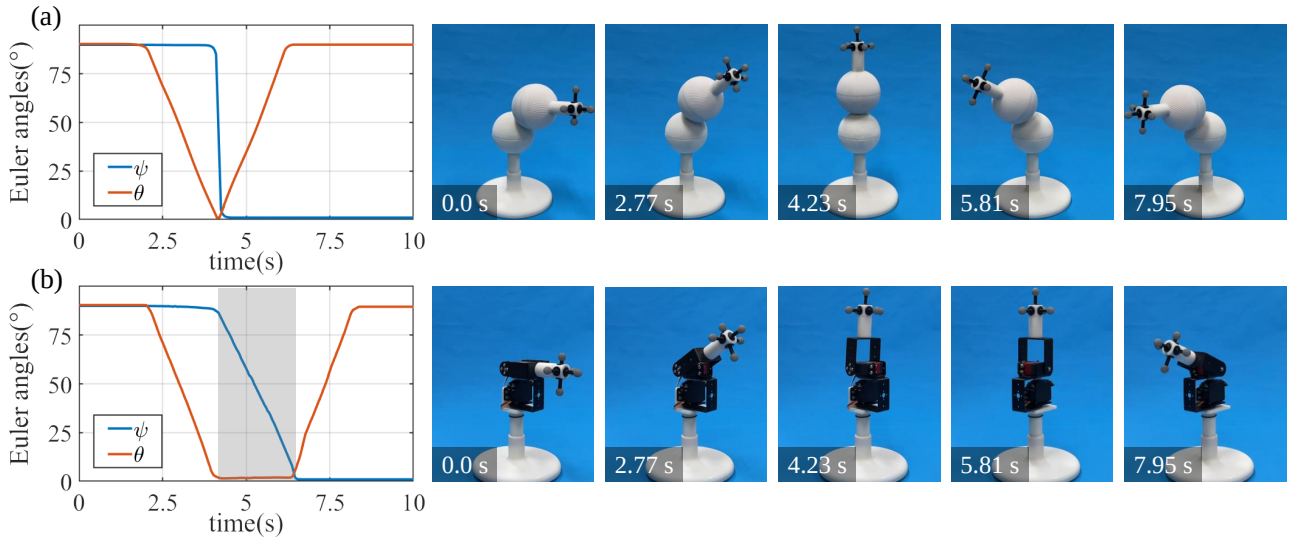

Fig. 20: Comparison of the proposed DISG-based robot wrist with a conventional 2-DoF wrist on singularities. (a) the DISG-based robot wrist passes through the reference configuration without singularities; (b) the conventional 2-DoF wrist encounters singularities and must adjust the azimuth ψ before continuing to the next configuration of motion.

D. 3-DoF independent robotic wrist extension

As an extended application, a 3-DoF robotic wrist with a full-range workspace is realized by connecting a revolute joint in series after DISG. A DC motor with an encoder is mounted on the end of the DISG-based rolling contact joint, together forming a 3-DoF wrist in a hybrid RC-R (rolling contact-revolute) configuration, as shown in Fig. 17. The 3-DoF robotic wrist configuration is characterized by azimuth ψ, evaluation θ, and yaw ϕ, as shown in Fig. 18. The 3-DoF robotic wrist configuration is characterized by azimuth ψ, evaluation θ, and yaw ϕ, as shown in Fig. 18. In contrast to the 2-DoF wrist, where the yaw ϕ is determined for a given azimuth ψ and evaluation θ, in the 3-DoF wrist, these three Euler angles are independent.

To test the proposed 3-DoF robotic wrist, a control system scheme similar to the one used in previous experiments is

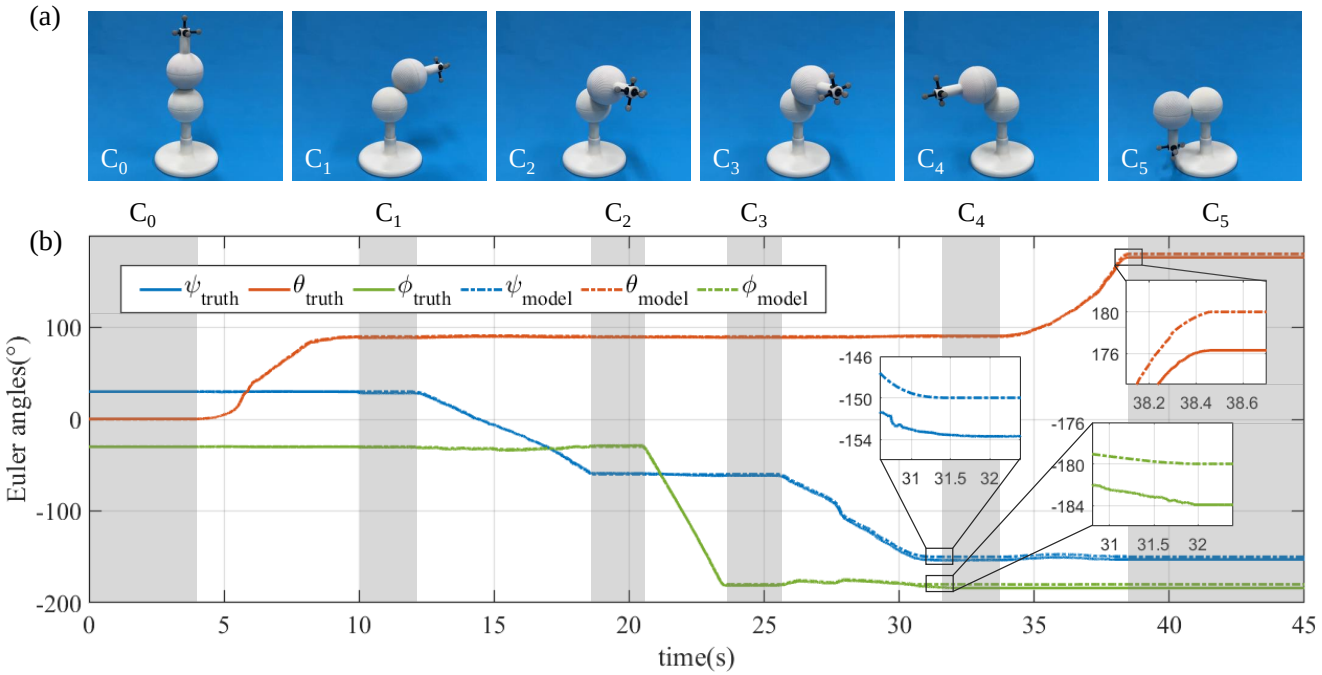

Fig. 21: A 3-DoF independent robotic wrist application based on DISG: during the 3-DoF wrist sequence through the reference configuration, (a) some motion frames captured at key moments and (b) euler angles characterizing orientation.

employed. Optical encoders mounted on the three motors (c_{1a}, c_{2a}, c_{3a}) measure the actual positions of the actively driving magnet, while the kinematic model is used to calculate the target encoder counts (c_{1t}, c_{2t}, c_{3t}) corresponding to the target configurations $(\psi_t, \theta_t, \phi_t)$. Two PID controllers are used for closed-loop position control of the RC joint and the additional revolute joint, respectively, based on the target inputs from the kinematics (c_{1t}, c_{2t}, c_{3t}) and the actual positions feedback from the encoders (c_{1a}, c_{2a}, c_{3a}). The controllers' PWM outputs are directly applied to drive the three DC motors.

Motion capture is used to measure the end pose of the proposed wrist, and several reference configurations are sequentially passed through, where only one Euler angle is changed in each configuration transformation, which are $C_1[30, 90, -30]^\circ$, $C_2[-60, 90, -30]^\circ$, $C_3[-60, 90, -180]^\circ$, $C_4[-150, 90, -180]^\circ$, and $C_5[-150, 180, -180]^\circ$. Fig. 21(a) shows some motion frames captured at key moments during the 3-DoF wrist sequence through the reference configuration. Fig. 21(b) displays the orientation of the end, including that measured by motion capture and calculated based on the kinematic model. The small error between the measured trajectory and the kinematic-based calculations again validates the correctness of the kinematic model. The experimental error observed in Fig. 21(b) is similar to that of previous experiments, with the primary factor being the cumulative error resulting from slight but uncontrollable slippage on the friction wheel. The results of the experiment indicate that the robotic wrist proposed is capable of independent movement in 3-DoF, whereby altering one Euler angle does not impact the other two. Moreover, the robotic wrist boasts a significant range of motion, encompassing the entire 3-DoF workspace.

E. DISG Control with Payload

The previous control approaches, which relied on kinematic models, predominantly focused on unloaded DISG. However, it has been observed that when subjected to both inertia and load, these methods exhibit inaccuracies arising from the intricate interplay among magnetic coupling pairs due to gravitational effects and dynamic factors in different configurations. To demonstrate the controllability of DISG performance in the presence of gravity and dynamics, an additional closed-loop control experiment was conducted using a loaded DISG with motion capture system.

In this experiment, a weight was attached to the end of the DISG. To mitigate the interference caused by reflected light during the motion capture process, the weight was covered with anti-reflective tape. Furthermore, several infrared reflective markers were affixed to the output link. These markers facilitated real-time measurement of the DISG's configuration by the motion capture system, providing accurate configuration regarding the effects of gravity and dynamics. Several reference configurations, specifically $C_1[10, 45]^\circ$, $C_2[-90, 45]^\circ$, and $C_3[30, 150]^\circ$, were established and sequentially traversed during the experiment. By utilizing the target configuration and real-time DISG configuration feedback obtained from motion capture, a closed-loop position control method employing a PID controller was utilized. The output from this controller was then used to actuate the actively driving magnet. For comparison purposes, an open-loop control case based on a kinematic model was also presented. Fig. 22 demonstrates the error, as measured by motion capture, between the real-time

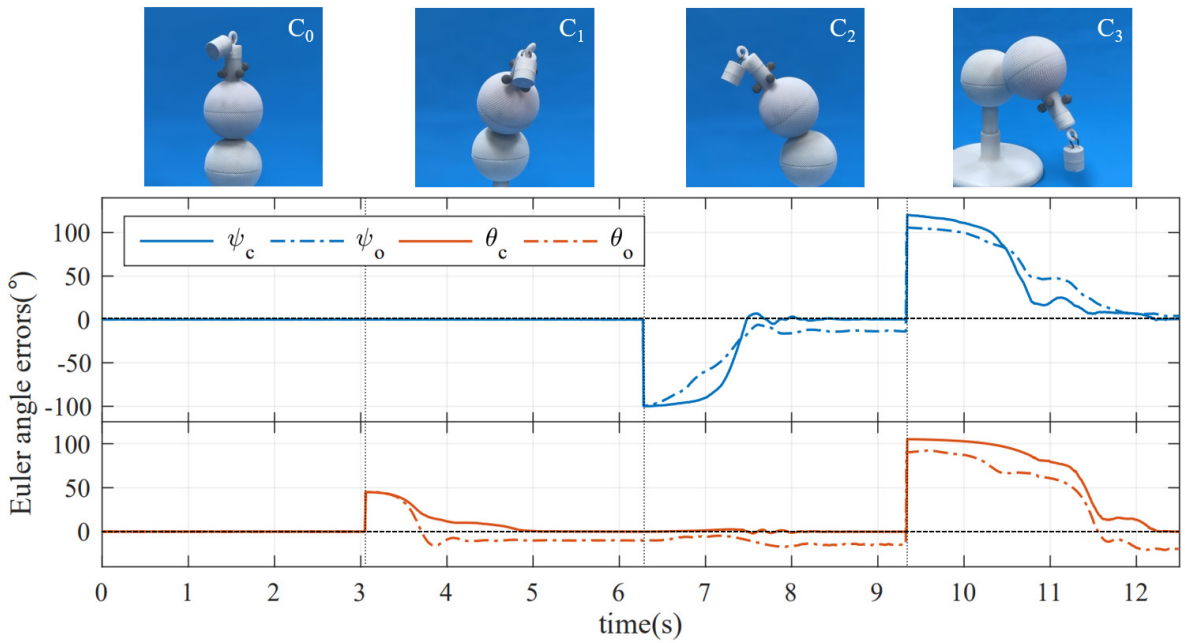

Fig. 22: The loaded DISG has undergone a series of predetermined reference configurations. The visual illustrations portray the errors observed in the Euler angle throughout the experimental tests. More precisely, the ψ_c and θ_c values represent the outcomes of closed-loop control, which were achieved by utilizing sensory feedback from the motion capture system. On the other hand, the corresponding ψ_o and θ_o values indicate the results of open-loop control, relying on the kinematic model.

Euler angles and the target Euler angles when the prototype passes through the reference configurations. The ψ_c and θ_c values represent the outcomes of closed-loop control, which were achieved by utilizing sensory feedback from the motion capture system. On the other hand, the corresponding ψ_o and θ_o values indicate the results of open-loop control, relying on the kinematic model. The images and videos clearly depict that, in the presence of a load, the movement of the DISG is noticeably less smooth compared to the unloaded scenario. Furthermore, significant control errors are observed when relying on open-loop control based on kinematics. In contrast, in the case of closed-loop control based on sensing feedback, although the motion exhibits fluctuations, the Euler angle error for each reference configuration tends to converge towards zero. The experimental results demonstrate the effectiveness of controlling a loaded DISG.

VI. Discussion

A. Comparison among representative joints

Table II and Fig. 23 were presented to compare several representative robotic wrists. The results indicate that our proposed DISG-based joint provides advantages in terms of motion range, dexterity, compactness, and lightweight when compared to other existing robotic wrists. Particularly, our proposed design surpasses all the existing wrists in terms of motion range, making it highly attractive for applications requiring a large workspace. One potential drawback of our proposed DISG-based joint is its low torque transfer capacity. However, this limitation can be addressed by incorporating enhanced passively following magnet, which can augment the joint's force and torque output.

B. Drive characteristics of DISG

The DISG exhibits distinct driving characteristics from conventional joints, as its joint configuration is determined by the interplay between the drive and load. In the DISG system, the magnet pair configuration governs the torque. Fig. 13 shows the relationship between the magnetic torque and configuration, where it is evident that the magnet pair of coaxial relative position does not generate torque, while the magnet pair with non-coaxial state generates torque. When there is no load, no extra magnetic torque is needed to counteract the load torque, resulting in a magnet coaxial pair configuration that represents a state of balance. Conversely, when a load is present, the magnet pair must generate magnetic torque via orientation error to balance the load torque, making a noncoaxial magnet pair configuration the state of balance. Considering this trait, the present study employs an external motion capture system to achieve closed-loop position control of the loaded DISG prototype. To augment the manipulation potential of DISG, our forthcoming investigations will center around creating a self-reliant attitude and heading reference system (AHRS) for DISG, thereby removing the need for the motion capture system. Additionally, we plan to embrace a more intricate control approach based on AHRS to amplify the performance of DISG even further.

C. Manufacturing of DISG

In this article, we are making the one-piece 3D tooth structure of DISG by 3D printing processing method. Specifically, we utilized 3D printing resin material to produce a spherical gear prototype. As it is well-known, 3D printing technology

TABLE II: COMPARISON AMONG REPRESENTATIVE WRISTS

Name	DoF	Wrist Configur.	Motion Range $\psi(^\circ)$	$\theta(^\circ)$	$\phi(^\circ)$	Weight (gram)	Torque (N · m)
Ours	2	RC	**360**	**180**	-	287.5	0.39
Kim [28]	2	RC	360	90	-	-	12.5
Sensinger [36]	2	R-R	360	90	-	619	2.2
Ours	3	RC-R	**360**	**180**	**360**	312.8	0.39
Kim [28]	3	RC-R	360	90	360	-	12.5
Abe [7]	3	S	270	90	360	-	0.4
Hess [37]	3	R-R-R	140	140	360	-	-
Bai [6]	3	S	60	30	360	1860	1.5
Gosselin [38]	3	R-R-R	140	140	30	-	0.42
Birglen [39]	3	R-R-R	90	45	90	6510	0.16
Kaneko [40]	3	S	30	30	360	4900	0.6
Yano [41]	3	S	90	90	360	-	2.06

R - revolute joint, S - spherical joint, RC - rolling contact joint.

offers advantages such as accuracy, affordability, rapidity, and the ability to produce complex structures in one piece. These features make it especially suited for manufacturing intricate 3D tooth structures in DISG. Notably, the machining accuracy of the tooth shape is crucial to ensure perfect meshing between two spherical gears. Otherwise, discontinuous transmission and jerky motion may result.

Furthermore, we enhanced the performance of DISG by treating the inner wall. On the side where the passively following magnet is located, we applied lubricant to minimize friction between the passively following magnet caster and the inner wall, enabling the passive magnet to follow the motion of the actively driving magnet smoothly. On the other side, where the actively driving magnet is located, we added a layer of non-slip tape to maximize the friction between the friction wheel and the inner wall, preventing the trolley from slipping inside the sphere.

However, current 3D printing technology has limitations such as weak strength and easy deformation. Although the prototype spherical gears made of resin were in good condition for the corresponding experiments, as mentioned earlier, there was minor slippage and wear between the two spherical gears in DISG, and the resin's strength deficiencies may become apparent after prolonged use. To expand DISG to a broader range of industrial applications, metal 3D printing, stamping, and casting methods could be considered, as they have the potential to create a stronger and more durable spherical gear structure.

VII. CONCLUSION

Dexterous joints have attracted the interest in the field of robotics. This paper presents a design for driving-integrated spherical gears that enables global meshing and active drive between two spherical gears, resulting in a dexterous multiDoF rolling contact joint. The kinematics of this design is thoroughly analyzed, and it is proven that the proposed DISG-based dexterous joint has good kinematic characteristics, including singularity-free and full-range workspace. To verify the characteristics of DISG, a series of experiments are conducted. The comparison results with other joint actuators

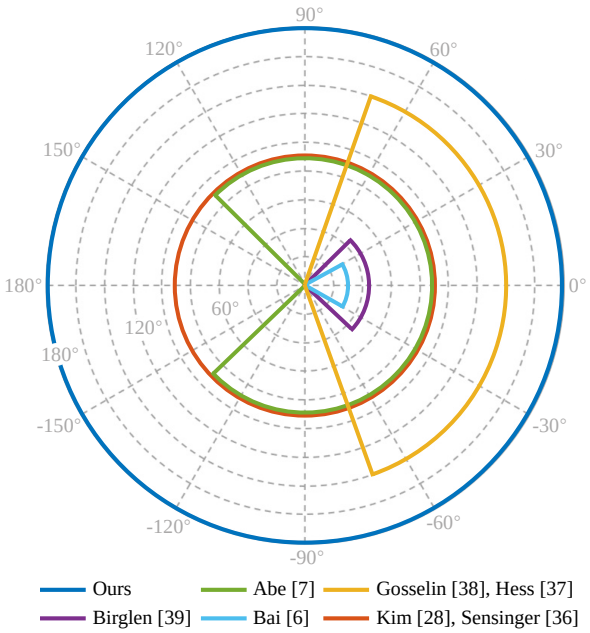

Fig. 23: Motion range of representative wrists

show that the DISG-based joints provides advantages in terms of motion range, dexterity, compactness, and lightweight.

In the forthcoming study, we intend to investigate the utilization of the AHRS within the context of DISG, aiming to eliminate reliance on motion capture systems for accurate joint localization. Building upon our prior work with configuration detection[42] on the modular robot FreeBOT[43, 44], integrating 3D Hall-effect sensors within the sphere holds promise for realizing real-time orientation tracking of passive magnets¡ªa key solution for the envisioned DISG AHRS. We aspire to enhance processing technology through improved materials and manufacturing, resulting in better motion performance. Our aspiration is for DISG to evolve into an integrated dexterous joint, incorporated into an array of robotic systems and smart devices in the times ahead.

APPENDIX A
DERIVATIONS OF VARYING CROSSING ANGLE BEVEL GEAR MATHMATICAL MODEL

In this section, we derive the mathematical model for bevel gears with varying crossing angles. To begin, we reference [35] and derive the mathematical model for bevel gears with constant crossing angles. In Fig. 24, the great circle remains in constant tangential contact with a base cone while rolling purely on it. The trajectory of point P on the great circle follows an involute curve represented by $\widehat{PQ}$. ΣS_0 is in the great circle, ΣS_1 is obtained by rotating ΣS_0 around the y_0 axis by an angle φ, ΣS_2 is obtained by rotating ΣS_1 around the x_1 axis by an angle γ, and ΣS_3 is on the base cone.

The point P in ΣS_0 is represented as

$$\boldsymbol{r}_0^{(p)} = \begin{bmatrix} 0 \\ 0 \\ r_0 \\ 1 \end{bmatrix}. \tag{26}$$

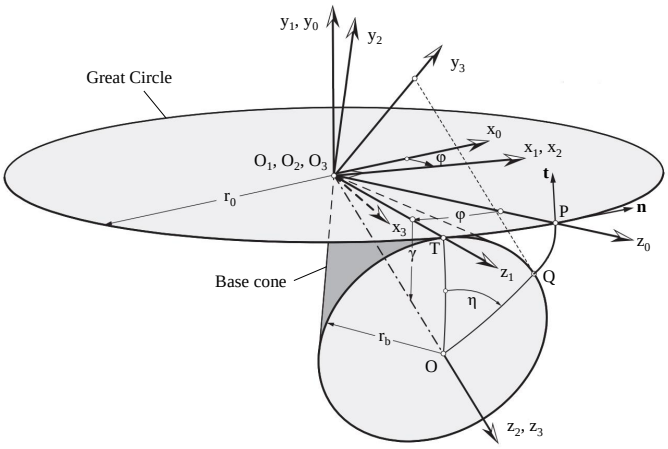

Fig. 24: Schematic representation of the generation of the involute profile using the coordinate transformation method.

The transformation matrix of ΣS_0 to ΣS_3 can be calculated as Eq. (27).

The point P expressed in ΣS_3 is the involute equation of the bevel gear with constant base cone angle (γ is a constant):

$$\boldsymbol{r}_s^{(p)} = \boldsymbol{T} \cdot \boldsymbol{r}_0^{(p)} = \begin{bmatrix} r_0\left(\cos\eta\sin\varphi - \sin\eta\cos\varphi\sin\gamma\right) \\ r_0\left(\sin\eta\sin\varphi + \cos\eta\cos\varphi\sin\gamma\right) \\ r_0\cos\varphi\cos\gamma \\ 1 \end{bmatrix}, \tag{28}$$

where r_0 is the radius of the great circle and also the radius of the base sphere of the spherical gear, η is the involute roll angle, and γ is the base cone angle.

By adjusting the angle at which two spherical bevel gears intersect (base cone angle γ), the rolling motion that occurs in the latitudinal direction can be seen as a pure rolling motion between a pair of pitch cones with changes in the cone angle, as depicted in Fig. 3(c). In this figure, $\overline{OA}$ denotes the polar axis of the spherical gear and has a length of L. $\overline{AB}$ represents the generatrix of both the base cone and the pitch cone, with a length of ρ. $\overline{OB}$ is the radius of the pitch sphere of the bevel spherical gear and has a length of r_b. The pitch cone angle is denoted by γ, which is the angle between $\overline{OA}$ and $\overline{AB}$, while β is the angle between $\overline{OA}$ and $\overline{OB}$, representing the latitude of the spherical bevel gear.

In Fig. 3(c), according to the Pythagorean theorem, we can see that in the $\triangle OAB$,

$$\begin{cases} \gamma + \beta = \frac{\pi}{2} \\ \rho_{(\beta)} = r_b \tan\beta \\ L_{(\beta)} = \frac{r_b}{\sin\gamma} = \frac{r_b}{\cos\beta} \end{cases}. \tag{29}$$

Then the parametric equation of the involute of the spherical bevel gear is the representation of the point P expressed in ΣS_4:

$$\begin{aligned} \boldsymbol{r}^{(s)}(\beta,\eta) &= \left[\begin{array}{c:c} Rot_y(\pi)Rot_z(-\frac{\pi}{2}) & \begin{matrix}0\\0\\L_{(\beta)}\end{matrix} \\ \hdashline \begin{matrix}0 & 0 & 0\end{matrix} & 1 \end{array}\right] \cdot \boldsymbol{r}_s^{(p)} \\ &= \begin{bmatrix} \rho_{(\beta)}\left(\sin\eta\sin\varphi + \cos\eta\cos\varphi\sin\gamma\right) \\ \rho_{(\beta)}\left(\cos\eta\sin\varphi - \sin\eta\cos\varphi\sin\gamma\right) \\ -\rho_{(\beta)}\cos\varphi\cos\gamma + L_{(\beta)} \\ 1 \end{bmatrix}. \end{aligned} \tag{30}$$

Therefore, for the structure of a spherical bevel gear with variable crossing angle, the involute can be rewritten as a two-parameter vector (β and η) with the equation as

$$\mathbf{r}^{(s)} = \boldsymbol{r}^{(s)}(\beta,\eta) = x(\beta,\eta)\mathbf{i} + y(\beta,\eta)\mathbf{j} + z(\beta,\eta)\mathbf{k}. \tag{31}$$

REFERENCES

[1] N. M. Bajaj, A. J. Spiers, and A. M. Dollar, "State of the art in artificial wrists: a review of prosthetic and robotic wrist design," *IEEE Transactions on Robotics*, vol. 35, no. 1, pp. 261–277, 2019.

[2] B. Siciliano and O. Khatib, *Springer handbook of robotics*. Springer, 2016, pp. 13–31.

[3] F. Montagnani, M. Controzzi, and C. Cipriani, "Is it finger or wrist dexterity that is missing in current hand prostheses?" *IEEE Transactions on Neural Systems and Rehabilitation Engineering*, vol. 23, no. 4, pp. 600–609, 2015.

[4] S. E. Wright, A. W. Mahoney, K. M. Popek, and J. J. Abbott, "The spherical-actuator-magnet manipulator: A permanent-magnet robotic end-effector," *IEEE Transactions on Robotics*, vol. 33, no. 5, pp. 1013–1024, 2017.

[5] K.-M. Lee and C.-K. Kwan, "Design concept development of a spherical stepper for robotic applications," *IEEE Transactions on Robotics and Automation*, vol. 7, no. 1, pp. 175–181, 1991.

[6] K. Bai, W. Chen, K.-M. Lee, Z. Que, and R. Huang, "Spherical wrist with hybrid motion-impedance control for enhanced robotic manipulations," *IEEE Transactions on Robotics*, vol. 38, no. 2, pp. 1174–1185, 2021.

[7] K. Abe, K. Tadakuma, and R. Tadakuma, "Abenics: Active ball joint mechanism with three-dof based on spherical gear meshings," *IEEE Transactions on Robotics*, vol. 37, no. 5, pp. 1806–1825, 2021.

$$\begin{aligned} \boldsymbol{T} &= \left[\begin{array}{c:c} Rot_z(-\eta) & \begin{matrix}0\\0\\0\end{matrix} \\ \hdashline \begin{matrix}0 & 0 & 0\end{matrix} & 1 \end{array}\right] \cdot \left[\begin{array}{c:c} Rot_x(\gamma) & \begin{matrix}0\\0\\0\end{matrix} \\ \hdashline \begin{matrix}0 & 0 & 0\end{matrix} & 1 \end{array}\right] \cdot \left[\begin{array}{c:c} Rot_y(-\varphi) & \begin{matrix}0\\0\\0\end{matrix} \\ \hdashline \begin{matrix}0 & 0 & 0\end{matrix} & 1 \end{array}\right] \\ &= \begin{bmatrix} \cos\eta\cos\varphi + \sin\eta\sin\varphi\sin\gamma & -\sin\eta\cos\gamma & \cos\eta\sin\varphi - \sin\eta\cos\varphi\sin\gamma & 0 \\ \sin\eta\cos\varphi - \cos\eta\sin\varphi\sin\gamma & \cos\eta\cos\gamma & \sin\eta\sin\varphi + \cos\eta\cos\varphi\sin\gamma & 0 \\ -\sin\varphi\cos\gamma & -\sin\gamma & \cos\varphi\cos\gamma & 0 \\ 0 & 0 & 0 & 1 \end{bmatrix}. \end{aligned} \tag{27}$$

[8] J. Z. Deninson, "Vericle," Sep. 26 1933, US Patent 1,928,412.

[9] W. H. Isely, "Control apparatus," Aug. 23 1966, US Patent 3,267,755.

[10] A. Kimura, M. Matsuzaki, A. Tanaka, and M. Inoue, "Lens frame supporting mechanism," Mar. 26 1996, US Patent 5,502,598.

[11] M. Kumaga and T. Ochiai, "Development of a robot balanced on a ball - application of passive motion to transport," in *IEEE International Conference on Robotics and Automation*. IEEE, 2009, pp. 4106–4111.

[12] M. E. Rosheim and G. F. Sauter, "New high-angulation omnidirectional sensor mount," in *Free-space laser communication and laser imaging II*, vol. 4821. SPIE, 2002, pp. 163–174.

[13] B. Zhuming, H. Xinyan, and L. Xiaoning, "Quasi-ellipsoidal gear drive used in the flexible joint of robot," in *IEEE International Conference on Robotics and Automation (ICRA)*. IEEE, 1996, pp. 1300–1305.

[14] Q. Jiang, Zhouji, and H. Li, "The design of quasi-ellipsoidal gear ratio and pitch curved surfaces," *Journal of Mechanical Design*, vol. 120, no. 2, pp. 364–367, 1998.

[15] L. Hu ran, "A new kind of spherical gear and its application in a robot's wrist joint," *Robotics and Computer Integrated Manufacturing*, vol. 25, no. 4-5, pp. 732–735, 2009.

[16] S.-C. Yang, "A rack-cutter surface used to generate a spherical gear with discrete ring-involute teeth," *The International Journal of Advanced Manufacturing Technology*, vol. 27, no. 1, pp. 14–20, 2005.

[17] H.-C. Yang, "Using an imaginary planar rack cutter to create a spherical gear pair with continue involute teeth," *Arabian Journal for Science and Engineering*, vol. 42, no. 11, pp. 4725–4735, 2017.

[18] L. Ting and P. Cunyun, "On grinding manufacture technique and tooth contact and stress analysis of ring-involute spherical gears," *Mechanism and Machine Theory*, vol. 44, no. 10, pp. 1807–1825, 2009.

[19] D. K. Park, "Pair of semi-spherical bevel gears," Jul. 14 1992, US Patent 5,129,275.

[20] Oskar van Deventer, "Spherigear transmission," https://www.shapeways.com/product/ET9RCZ2E2/spherigear-transmission, 2020.

[21] K. Tadakuma, R. Tadakuma, K. Ioka, T. Kudo, M. Takagi, Y. Tsumaki, M. Higashimori, and M. Kaneko, "Study on the omnidirectional driving gear mechanism," in *2012 IEEE International Conference on Robotics and Automation*. IEEE, 2012, pp. 3531–3532.

[22] R. Tadakuma, K. Tadakuma, and E. F. M. Arimie, "Study on omnidirectional driving mechanisms to realize holonomic power transmission," in *MHS2013*. IEEE, 2013, pp. 1–5.

[23] K. Abe, G. Matsui, K. Tadakuma, M. Yamano, and R. Tadakuma, "Development of the omnidirectional transporting table based on omnidirectional driving gear," *Advanced Robotics*, vol. 34, no. 6, pp. 358–374, 2020.

[24] K. Tadakuma, H. Saito, K. Abe, S. Hao, and R. Tadakuma, "Study on mechanism of spherical omnidirectional driving gear with two degrees of freedom," *Journal of the Robotics Society of Japan*, vol. 36, no. 9, pp. 627–638, 2018.

[25] L. Cui and J. S. Dai, "A darboux-frame-based formulation of spin-rolling motion of rigid objects with point contact," *IEEE Transactions on Robotics*, vol. 26, no. 2, pp. 383–388, 2010.

[26] Z. Li and J. Canny, "Motion of two rigid bodies with rolling constraint," *IEEE Transactions on Robotics and Automation*, vol. 6, no. 1, pp. 62–72, 1990.

[27] L. Zong, G. Liang, and T. L. Lam, "Kinematics modeling and control of spherical rolling contact joint and manipulator," *IEEE Transactions on Robotics*, vol. 39, no. 1, pp. 738–754, 2023.

[28] Y.-J. Kim, "Anthropomorphic low-inertia high-stiffness manipulator for high-speed safe interaction," *IEEE Transactions on Robotics*, vol. 33, no. 6, pp. 1358–1374, 2017.

[29] M. G. Catalano, G. Grioli, E. Farnioli, A. Serio, C. Piazza, and A. Bicchi, "Adaptive synergies for the design and control of the pisa/iit softhand," *The International Journal of Robotics Research*, vol. 33, no. 5, pp. 768–782, 2014.

[30] C. Della Santina, C. Piazza, G. Grioli, M. G. Catalano, and A. Bicchi, "Toward dexterous manipulation with augmented adaptive synergies: The pisa/iit softhand 2," *IEEE Transactions on Robotics*, vol. 34, no. 5, pp. 1141–1156, 2018.

[31] J.-M. Boisclair, T. Laliberté, and C. Gosselin, "On the optimal design of underactuated fingers using rolling contact joints," *IEEE Robotics and Automation Letters*, vol. 6, no. 3, pp. 4656–4663, 2021.

[32] J. Kim, S.-i. Kwon, Y. Moon, and K. Kim, "Cable-movable rolling joint to expand workspace under high external load in a hyper-redundant manipulator," *IEEE/ASME Transactions on Mechatronics*, 2021.

[33] Y. Hu, L. Zhang, W. Li, and G.-Z. Yang, "Design and fabrication of a 3-d printed metallic flexible joint for snake-like surgical robot," *IEEE Robotics and Automation Letters*, vol. 4, no. 2, pp. 1557–1563, 2019.

[34] J.-w. Suh, K.-y. Kim, J.-w. Jeong, and J.-j. Lee, "Design considerations for a hyper-redundant pulleyless rolling joint with elastic fixtures," *IEEE/ASME Transactions on Mechatronics*, vol. 20, no. 6, pp. 2841–2852, 2015.

[35] A. Fuentes-Aznar and I. Gonzalez-Perez, "Mathematical definition and computerized modeling of spherical involute and octoidal bevel gears generated by crown gear," *Mechanism and Machine Theory*, vol. 106, pp. 94–114, 2016.

[36] T. Lenzi, J. Lipsey, and J. W. Sensinger, "The ric arm - a small anthropomorphic transhumeral prosthesis," *IEEE/ASME Transactions on Mechatronics*, vol. 21, no. 6, pp. 2660–2671, 2016.

[37] T. A. Hess-Coelho, "A redundant parallel spherical mechanism for robotic wrist applications," *ASME Journal of Mechanical Design*, vol. 129, no. 8, pp. 891–895, 2007.

[38] C. M. Gosselin and E. St-Pierre, "Development and

experimentation of a fast 3-dof camera-orienting device," *The International Journal of Robotics Research*, vol. 16, no. 5, pp. 619–630, 1997.

[39] L. Birglen, C. Gosselin, N. Pouliot, B. Monsarrat, and T. Laliberté, "Shade, a new 3-dof haptic device," *IEEE Transactions on Robotics and Automation*, vol. 18, no. 2, pp. 166–175, 2002.

[40] K. Kaneko, I. Yamada, and K. Itao, "A spherical dc servo motor with three degrees of freedom," *ASME Journal of Dynamic Systems, Measurement, and Control*, vol. 111, no. 3, pp. 398–402, 1989.

Guanqi Liang (Student Member, IEEE) received the B.S. degree in electrical engineering and automation from the China University of Mining and Technology, Jiangsu, China, in 2019. He is currently working toward the Ph.D. degree with the Chinese University of Hong Kong, Shenzhen, China.

His main research interests include modular self-reconfigurable robotics and mechanism.

Mr. Liang received the IROS Best Paper Award on Robot Mechanisms and Design in 2020.

Lijun Zong (Member, IEEE) received the B.S. degree in detection, guidance, and control technology from the Beijing Institute of Technology, Beijing, China, in 2013, and the M.S. and Ph.D. degrees in flight vehicle design from the Northwestern Polytechnical University, Xi'an, China, in 2015 and 2020, respectively.

He worked as a visiting scholar with the University of Toronto, Canada in 2016–2018, and a Postdoctoral Fellow with the Chinese University of Hong Kong, Shenzhen, China during 2020–2022. He is currently an Associate Professor with the Northwestern Polytechnical University, Xi'an, China. His research interests include space manipulators and modular self-reconfigurable robots.

[41] T. Yano, T. Suzuki, M. Sonoda, and M. Kaneko, "Basic characteristics of the developed spherical stepping motor," in *IEEE/RSJ International Conference on Intelligent Robots and Systems (IROS), Kyongju, South Korea*, 1999: 1393–1398.

[42] Y. Tu, G. Liang, and T. L. Lam, "Graph convolutional network based configuration detection for freeform modular robot using magnetic sensor array," in *2021 IEEE International Conference on Robotics and Automation (ICRA)*. IEEE, 2021, pp. 4252–4258.

[43] G. Liang, H. Luo, M. Li, H. Qian, and T. L. Lam, "Freebot: A freeform modular self-reconfigurable robot with arbitrary connection point-design and implementation," in *IEEE/RSJ International Conference on Intelligent Robots and Systems (IROS), Las Vegas, USA*, 2020: 6506-6513.

[44] T. L. Lam and G. Liang, "Self-reconfigurable robot module and self-reconfigurable robot," Jul. 8 2021, US Patent App. 17/134,066.

Tin Lun Lam (Senior Member, IEEE) received the B.Eng. (First Class Hons.) and Ph.D. degrees in robotics and automation from the Chinese University of Hong Kong, Hong Kong, in 2006 and 2010, respectively.

He is currently an Assistant Professor with the Chinese University of Hong Kong, Shenzhen, China, the Executive Deputy Director of the National-Local Joint Engineering Laboratory of Robotics and Intelligent Manufacturing, and the Director of Center for the Intelligent Robots, Shenzhen Institute of Artificial Intelligence and Robotics for Society. His research interests include multirobot systems, field robotics, and collaborative robotics.

Dr. Lam received the IEEE/ASME TRANSACTIONS ON MECHATRONICS Best Paper Award in 2011 and the IROS Best Paper Award on Robot Mechanisms and Design in 2020.